Tampere University

Farhad Ghasemzadeh

ENHANCED TRANSMISSION VIA EPSILON-NEAR-ZERO METAMATERIAL

Master of Science Thesis
Faculty of Natural Sciences
Examiners: Assoc. Prof. Humeyra Caglayan
Ph.D. Alireza Rahimi Rashed
May 2020

ABSTRACT

Farhad Ghasemzadeh: Enhanced transmission via epsilon-near-zero metamaterial
Master of Science Thesis
Tampere University
Degree Programme
May 2020

Epsilon-Near-Zero (ENZ) metamaterials, including both natural and fabricated, has been a hot topic of studies in recent twenty years. Theoretical background for ENZ metamaterials and their properties such as phase conservation or static behavior of the propagating dynamic electromagnetic field are investigated thoroughly. Functional capabilities such as uses in phase front engineering, subwavelength lensing, isolation of optical signals, super coupling, and high nonlinearly are proposed and found practical applications.

The purpose of this thesis was to design, study, and interpret the extraordinary transmission (EOT) of light in subwavelength apertures placed over ENZ metamaterials. The ENZ metamaterials are utilized to enhance the polarized light through different apertures. The physics and mechanisms behind the observed transmission enhancement are often overlooked or may not be accurate. This study is an effort to reveal the nature of the mentioned phenomena using both theoretical and experimental methods.

A background for optical concepts such as optical properties of ENZ metamaterials, hybridization of propagating and localized surface plasmons in a metallic aperture, and optical behavior of subwavelength apertures are presented. The simulation, fabrication, and characterization procedures of designed samples are briefed. A presentation of simulations and physical explanation for underlying mechanisms behind the nature of the observed EOT of light through ENZ based subwavelength apertures are analyzed precisely. Moreover, the fabricated samples and detailed measurements are presented and compared with simulation results. The acquired results are in a good agreement with predictions and simulations. Fabrication of several slits (more than four) and other 3D apertures remains as an open chapter for further studies.

Keywords: metamaterials, epsilon-near-zero, ENZ, subwavelength aperture, Extraordinary transmission, EOT, phase engineering, ITO, plasmonics, plasmon hybridization, LSP, PSP

PREFACE

This master's thesis was guided and written under the supervision of Associate Professor Caglayan and Ph.D. Alireza Rahimi Rashed in Tampere University, Finland.

I would like to offer special thanks to my supervisor Prof. Caglayan and Dr. Rashed, for guiding me with patience and helping with all the steps. Their instructive and close supervision helped me to gain a profound understanding of the research. Collaborating in an international group prepared me to work in similar groups. The value of this experience and work is unfathomable, and I am thankful for it, which extends much beyond only the research and studies. I would like to extend my gratitude to Dr. Bilge Can Yildiz for her help in simulations and providing insights.

I would like to express my thankfulness for the possibility of a free education provided for me in Finland. I also express my sincere gratitude to researchers and doctoral students for their help. It was a privilege to work with them and learn all the way. Finishing this thesis was not possible without the help of them. I expand my gratitude to all my previous teachers, supervisors, and co-workers that helped me to overcome challenges and open up a new window toward a better future. I dedicate my graduation to the most influential persons in my life; thanks, Mom and Dad, for encouraging and supporting me always. A special thanks to my sister and my Aunt, who motivated me to turn hardships to opportunities. I like to thank all my friends for their warm companionship. I like to express gratitude to all Wikipedia writers and FOSS software and open source creators.

I started this thesis in early February this year. Every other week that has past we faced a new situation due to "the Coronavirus pandemic". This situation required many changes and adaptations. Whole-time I remembered a quote that my father said during my childhood, and Steven Hawking also articulates it as "Intelligence is the ability to adapt to change.", now after almost three months, I realize new challenges bring possibilities and blessings. I would like to finish this preface by reminding myself and others that every moment that we have is precious and unique, and we should take advantage of it.

Tampere, 7th May 2020

Farhad Ghasemzadeh

CONTENTS

LIST OF FIGURES

LIST OF SYMBOLS AND ABBREVIATIONS

1D	One dimensional
2D	Two dimensional
3D	Three dimensional
A	Amplitude
A	Absorption
ATR	Attenuated Total Reflection
$\mathbf{B}$	Magnetic flux density
c_0	Speed of light in vacuum
$\mathbf{D}$	Electric flux density
EOT	Extraordinary Optical Transmittance
E_0	Amplitude of an electric field
e	unit of electric charge, equal to $1.602176634 \times 10^{-19}$
$\mathbb{E}$	Electric field
EM	Electromagnetic
ENZ	Epsilon Near Zero
F	Farad is the SI derived unit of electrical capacitance
f	Frequency
$\mathcal{F}[a(t)]$	The Fourier transform of the function a
FDTD	The Finite Difference Time Domain method
FIB	Focused Ion Beam
FOSS	Free and open source software
$\mathbb{H}$	Magnetic field
H	Henry is the SI unit of electrical inductance
HMM	Hyperbolic metamaterials
I	Intensity
i	Unit imaginary number
Im, Imag	Imaginary part
i.e.	Latin abbreviation for id est, used to explain, clarify or rephrase a statement

I_0	Initial intensity
ITO	Indium Tin Oxide
j	Electric current density
$\mathbf{K}$	Complex extinction coefficient
$\mathbf{k}$	Wavevector
k	Wavenumber
k_i	Wavenumber along i axis
k_0	Wavenumber in vacuum
LCP	Left-hand circular polarized
l	Optical path
LCD	Liquid Crystal Display
LSP	Localized surface plasmon
m	The base unit of length in SI
MATLAB	Matrix laboratory
m_e	Effective mass of electron
MNZ	Mu Near Zero
N	Number of atoms per unit volume
n	Refractive index
NIR	Near-infrared
OLED	Organic Light-Emitting Diode
PA	Perfect Absorption
PEC	Perfect Electrical Conductor
PMC	Perfect Magnetic Conductor
$\mathbb{P}$	Electric polarization
PSP	Propagating Surface Plasmon
RCP	Right-hand circular polarized
RIE	Reactive Ion etching
$\mathbf{r}$	Position vector
$\mathbf{S}$	Poynting's vector
SI system	International system of units (Système international d'unités in French)
s	The second is the SI unit of time
SEM	Scanning Electron Microscope
SPP	Surface Plasmon Polariton

t	Time
TCO	Transparent Conductive Oxide
TE	Transverse Electric
TM	Transverse Magnetic
v_p	Phase velocity
v_g	Group velocity
Watt	Unit of power
wt	Mass fraction
ZIM	Zero-index-material
α	Attenuation coefficient
Γ_{bulk}	Collision frequency
ϵ_0	Permittivity of vacuum
ϵ	Relative permittivity
ϵ'	Real part of relative permittivity
ϵ_{real}	Real part of relative permittivity
ϵ''	Imaginary part of relative permittivity
ϵ_{imag}	Imaginary part of relative permittivity
ϵ_∞	Background permittivity
ϵ_{Drude}	Drude permittivity
$\epsilon_m(\omega)$	Frequency dependent permittivity
$\epsilon_\parallel$	Parallel part of effective permittivity in a multilayer structure
$\epsilon_\perp$	Perpendicular part of effective permittivity in a multilayer structure
ϵ_{eff}	Effective permittivity
η_0	Characteristic impedance of vacuum
θ_1	The incident angle
θ_2	The refraction angle
θ_c	Critical angle
κ	Extinction coefficient
λ_{ENZ}	ENZ wavelength
λ_0	Wavelength in vacuum
λ	Wavelength
μ_0	Permeability of vacuum
μ_r	Relative permeability, in this thesis it is always one
π	3.14159265358979323846

ρ	Metal fill fraction
τ	Mean free time between ionic collisions
χ''	Imaginary part of Susceptibility
χ'	Real part of Susceptibility
χ	Susceptibility
ω_p	Plasma frequency
ω_d	Collision frequency
ω	Angular frequency
Ω	The ohm is the SI unit of electrical resistance

1 INTRODUCTION

Metamaterials are optical structures that can control the electromagnetic wave's behavior and exhibit extraordinary optical properties. The realization of the first metamaterials returns to the medieval age which, can be found in artifacts such as the Lycurgus cup, doped with gold nanoparticles. This kind of primary application of metamaterials was limited to aesthetics utilization.
The first paper to investigate metamaterials is Bose's paper (1898) written about the physical properties of a twisted structure, which could change the plane of polarization of the light. Later, early studies include the possibility of an anti-parallel group and phase velocity by Lamb and Shuster in 1904 and a crystal lattice structure study by Mandelstam in 1945, which leads to a negative phase velocity demonstration in these crystalline structures. One chief cornerstone of this field was placed by Veselago in 1968 by publishing a theoretical work about negative refractive index and introducing a new term "left-handed materials". Veselago stated that, in order to obtain a left-handed material, relative permittivity and permeability of the material should simultaneously become negative. These kinds of metamaterials are now dubbed as double-negative metamaterials.
Epsilon-near-zero (ENZ) materials,i.e., materials with a zero permittivity, are natural or artificial structures that reveal an exotic behavior at a specific spectral range called ENZ wavelength. Several metals like silver and gold and transparent conductive oxides such as indium tin oxide and tin oxide have belonged to ENZ materials in their respective ENZ wavelength. However, even though ENZ material definition only obligates that real part of the permittivity to be zero, the imaginary part of the material at ENZ wavelength plays a crucial role. The high values of the imaginary part can hinder the functional applications of the ENZ metamaterials.

ENZ metamaterials, including both natural and fabricated, has been a hot topic of recent studies in these twenty years. Theoretical background for ENZ metamaterials and properties such as phase conservation or static behavior of the propagating dynamic electromagnetic field are investigated thoroughly. Functional capabilities such as uses in phase front engineering, subwavelength lensing, isolation of optical signals, super coupling and high non-linearly are proposed and found practical applications.
The need for further development of new devices based on ENZ metamaterials motivated us to use them as a mediator for enhancing extraordinary transmission (EOT) of light through subwavelength apertures. It is shown by Bethe [1] and later by Maier [2] that transmission of light from a subwavelength aperture is negligible. In recent studies, ENZ

metamaterials are used as nanostructure to facilitate the transmission of light through a slit [3]. However, in these studies the experimental realization of the designed structures remained challenging. On the other hand, revealing underlying physics and mechanisms behind the observed EOT through a subwavelength slit are overlooked.

The purpose of this thesis was to design, study, and interpret enhanced transmission of light in ENZ based subwavelength apertures. To achieve these goals, in the next chapter of this thesis, a background for optical concepts such as ENZ materials and their unique properties, hybridization of localized and propagating plasmons in a metallic aperture and optical behavior of subwavelength apertures are presented. The Methods chapter includes simulation, fabrication and characterization procedures of designed samples. Chapter four presents simulations and physical explanation for underlying mechanisms behind the nature of EOT of light through subwavelength apertures placed on an ITO thin film. Moreover, the fabricated samples and detailed measurements are presented and compared with simulation results. The last chapter includes a conclusion of this study and ideas for future projects.

2 BACKGROUND

In this chapter, optical constants, and Beer-Lambert law is explained as a foundation for latter parts. Epsilon-near-zero material is introduced and classified. The unusual behavior of Epsilon-near-zero material is briefly explained with examples and figures. As a final part, for the background, optical subwavelength aperture and extraordinary transmission in metamaterials are explained.

2.1 Optical Constants

To understand the optical constants, one should first know the constitutive relations. In electromagnetism constitutive relations in vacuum are defined as follows [4]:

$$\mathbf{D} = \epsilon_0 \mathbf{E}, \tag{2.1}$$

$$\mathbf{B} = \mu_0 \mathbf{H}, \tag{2.2}$$

where $\mathbf{D}$ is electric, and $\mathbf{B}$ is magnetic flux densities. $\mathbf{E}$, $\mathbf{H}$ are electric and magnetic fields, respectively. ϵ_0, μ_0 are permittivity and permeability, respectively; and numerically they correspond to:

$$\epsilon_0 = 8.85 \times 10^{-12} F/m$$

$$\mu_0 = 4\pi \times 10^{-7} H/m$$

Speed of light and characteristic impedance of vacuum is defined using ϵ_0 and μ_0:

$$c_0 = \frac{1}{\sqrt{\epsilon_0 \mu_0}} = 3 \times 10^8 m/s, \tag{2.3}$$

$$\eta_0 = \sqrt{\frac{\mu_0}{\epsilon_0}} = 337\Omega, \tag{2.4}$$

To write (2.1) and (2.2) equations inside a material, it is imperative to differentiate between various materials, and optical behavior of light inside the medium. For example, different materials can possess different properties such as isotropicity, homogeneity, which can manipulate the light differently. Isotropicity is a property that defines the uniformity of a material's parameter with respect to different orientations. Isotropicity in optics is defined

by the fact that if primitive field phasors of $\mathbf{E}$ and $\mathbf{E}$ are co-directional with induction field phasors of $\mathbf{D}$ and $\mathbf{H}$. Relative permittivity and permeability in such mediums are reduced to a scalar [5]. Unlike isotropic media, in anisotropic materials $\mathbf{E}$ and $\mathbf{B}$ are not aligned along $\mathbf{D}$ and $\mathbf{H}$. It is inevitable to adopt tensor calculus to calculate permittivity and permeability in anisotropic media. Magnetic medium is not the point of interest here, and (2.2) will preserve its form for anisotropic material as well $(\mu_r = 1)$. However the relation between $\mathbf{D}$ and $\mathbf{E}$ is defined differently:

$$\begin{bmatrix} D_x \\ D_y \\ D_z \end{bmatrix} = \begin{bmatrix} \epsilon_{xx} & \epsilon_{xy} & \epsilon_{xz} \\ \epsilon_{yx} & \epsilon_{yy} & \epsilon_{yz} \\ \epsilon_{zx} & \epsilon_{zy} & \epsilon_{zz} \end{bmatrix} \begin{bmatrix} E_x \\ E_y \\ E_z \end{bmatrix} \tag{2.5}$$

where D_x, D_y and D_z are electric flux densities in the direction of x,y and z-axis, respectively. Each of ϵ_{ij} are elements of the permittivity tensor and depend on the material's nature [6].

The formula (2.5) inside an isotropic material is written as [7]:

$$D = \epsilon E, \tag{2.6}$$

ϵ is the permittivity, and it is defined using susceptibility χ. Susceptibility is a complex function with a real dispersive part χ', and an absorptive imaginary part χ'':

$$\chi = \chi' + i\chi'', \tag{2.7}$$

The permittivity can be simplified as follows:

$$\epsilon = \epsilon_0(1 + \chi') + i\epsilon_0\chi'', \tag{2.8}$$

It is convenient to separate real and imaginary parts of relative primitively:

$$\epsilon' = \epsilon_0(1 + \chi'), \tag{2.9}$$

$$\epsilon'' = \epsilon_0\chi'', \tag{2.10}$$

The relative permittivity of dielectric materials is considered to be greater than one regardless of the frequency of the light [8]. For metals, the optical properties are different and depend on two facts [9]:

1. The electrons in the conduction band are from the bound of each atom or molecule and can freely move inside the balk material.
2. Interband excitations between the valence band and conduction band can only occur if the energy of the incident photons exceeds the bandgap between them in that

particular metal.

In the 20th century, a German physicist named Paul Drude, in an attempt to describe optics using Maxwell equations, used the kinetic theory of gasses to explain movements of electrons in metals. He used three assumptions:

1. There is no interaction between electrons and ions during collisions.
2. Electron-electron Scattering is neglected.
3. Collision probability per unit time for electrons is $\frac{1}{\tau}$, where τ is the interval time between two near collisions.

The induced electric polarization ($\boldsymbol{P}$) can be defined as the net average dipole moment per unit volume:

$$P = \varepsilon_0 \chi E \tag{2.11}$$

One can define the background permittivity (ϵ_∞) of a bulk medium, according to the electric polarization ($\boldsymbol{P}$) of the material which occurs as a response to the incident electric field:

$$\varepsilon_\infty = 1 + \frac{\boldsymbol{P}}{\varepsilon_0 \boldsymbol{E}} \tag{2.12}$$

This theory implies that the movement of the electron cloud is the sum of each electron's motion. One can solve the following motion equation to extract the frequency-depended displacement(x) of the free electrons in the space, as a response to the external electric field with an amplitude of E_0 and obtain:

$$m_e \frac{\partial^2 x}{\partial t^2} + m_e \omega_d \frac{\partial x}{\partial t} = e E_0 e^{-i\omega t} \tag{2.13}$$

where ω_d is the collision frequency, and m_e stands for the effective mass of the bound electrons. By substituting 2.12 in the differential equation of 2.13 one obtains the permittivity of material as follows:

$$\varepsilon_{\text{Drude}}(\omega) = \varepsilon_\infty - \frac{\omega_p^2}{\omega^2 + \omega_d^2} + i \frac{\omega_p^2 \omega_d}{\omega \left(\omega^2 + \omega_d^2\right)} \tag{2.14}$$

where $\varepsilon_{\text{Drude}}(\omega)$ is the permittivity at the frequency of ω, and ω_p is plasma frequency ($\omega_p = \frac{Ne^2}{\epsilon_0 m^*}$). The real part of equation 2.14 shows the group velocity dispersion, and the imaginary part is responsible for the dissipation of energy related to the motion of electrons in the material. According to Drude, free electrons exhibit a resonance absorption at the bulk plasmon frequency, meaning that they coherently oscillate in a phase when a time-dependent electric field is applied [10].

One can obtain the relation between refractive index (n) and relative permittivity (ϵ) by Fourier-decomposing the E function into exponential form and finding two components of

susceptibility regarding refractive index (n) and extinction coefficient (κ) :

$$Ae^{i(k_x x+k_y y+k_z z-\omega t)} \equiv Ae^{i(\mathbf{k}\cdot\mathbf{r}-\omega t)}, \quad \text{where} \quad \mathbf{k} \equiv (k_x, k_y, k_z) \tag{2.15}$$

where A is a real constant, k_i are wave vector elements (in one-dimensional case k becomes a wave number instead of wave vector), $\mathbf{k}$ is the wave vector, $\mathbf{r}$ is the position vector, ω is the angular frequency of E field, and t denotes the time.
Wave equation for an electric field is written as:

$$\frac{\partial^2 E_x}{\partial t^2} = \frac{1}{\mu_0\epsilon_0}\left(\frac{\partial^2 E_x}{\partial x^2} + \frac{\partial^2 E_x}{\partial y^2} + \frac{\partial^2 E_x}{\partial z^2}\right) \tag{2.16}$$

All the parameters used in this equation are the same as the ones defined earlier.
By plugging (2.15) into (2.16), the angular frequency is expressed as [11]:

$$-\omega^2 = \frac{1}{\mu_0\epsilon_0}\left(-k_x^2 - k_y^2 - k_z^2\right) \quad \Rightarrow \quad \omega^2 = \frac{|\mathbf{k}|^2}{\mu_0\epsilon_0} \quad \Rightarrow \quad \omega = c_0|\mathbf{k}| \tag{2.17}$$

The equation (2.17) can be solved for vacuum with a similar approach [12]. For a dielectric material it will become as:

$$\left(\frac{kc}{\omega}\right)^2 = 1 + \chi \tag{2.18}$$

Inside a medium $\frac{kc}{\omega}$ holds a complex value and can be written as:

$$\frac{kc}{\omega} = n + i\kappa \tag{2.19}$$

Here n is the real part of the refractive index of the medium, and κ is the extinction coefficient of the medium. From complex analysis and equation (2.18) components of susceptibility are written as [7]:

$$\epsilon_{real} = (n)^2 - (\kappa)^2 = (1 + \chi') \tag{2.20}$$

$$\epsilon_{imag} = 2n\kappa = \chi'' \tag{2.21}$$

For a loss-free material, only real parts are considered, and from 2.9 one can equate two as follows [7]:

$$(n)^2 - (\kappa)^2 = (1 + \chi') = \frac{\epsilon'}{\epsilon_0} \tag{2.22}$$

Similarly, for an absorptive material, the imaginary part exists as [7]:

$$2n\kappa = \chi'' = \frac{\epsilon''}{\epsilon_0} \tag{2.23}$$

Finally, the relation between refractive index(complex) and extinction coefficient and rela-

tive permittivity can be written as [7]:

$$n = n + i\kappa = \sqrt{(\frac{\epsilon'}{\epsilon_0}) + i(\frac{\epsilon''}{\epsilon_0})} = \sqrt{\epsilon} \tag{2.24}$$

where $\epsilon = (\frac{\epsilon'}{\epsilon_0}) + i(\frac{\epsilon''}{\epsilon_0})$ is known as relative permittivity of the medium which in literature it is often used as dielectric constant [13].

If k_0 is defined as the vacuum wavenumber and k is the material's wavenumber (propagation parameter), then the relative permittivity and propagation parameters related as [7, 14]:

$$k = 2\frac{\pi}{\lambda} = k_0 n = k_0\sqrt{\epsilon}, \quad \lambda = \frac{\lambda_0}{n} \tag{2.25}$$

where λ and λ_0 are wavelength inside material and vacuum respectively.

2.2 Beer-Lambert law

According to equations 2.14 and 2.24, one can write the refractive index of a medium as follows [15]:

$$\begin{aligned} n = n + ik =& 1 - \frac{Ne^2\left(\omega_0^2 - \omega^2\right)}{2\varepsilon_0 m\left[\left(\omega_0^2 - \omega^2\right)^2 + \Gamma_{bulk}^2\omega^2\right]} \\ &+ i\frac{Ne^2\Gamma_{bulk}\omega}{2\varepsilon_0 m\left[\left(\omega_0^2 - \omega^2\right)^2 + \Gamma_{bulk}^2\omega^2\right]} \end{aligned} \tag{2.26}$$

Where n is the refractive index, κ is the imaginary part of the refractive index, N is the number of atoms per unit volume for a medium,Γ_{bulk} the collision frequency, e is the electric charge, ω_0 is the resonant frequency of the electron and ω is the angular frequency. To explain the extinction coefficient (κ) and quantitative representation of the absorption, one can write the propagation of a plane wave inside a medium with a refractive index defined as 2.25 and achieve the following equations [16]:

$$\mathbf{E} = A\exp[i(\omega t - Kz)] \tag{2.27}$$

The equation 2.24 is written in a complex form as:

$$K = \frac{2\pi}{\lambda}(n + i\kappa) \tag{2.28}$$

Now the electric field is written as follows:

$$\mathbf{E} = A\exp\left[i\left(\omega t - \frac{2\pi n}{\lambda}z\right)\right]\exp\left(-\frac{2\pi\kappa}{\lambda}z\right) \tag{2.29}$$

In order to define the attenuation coefficient, one should first know the definition of intensity and the Poynting vector. The directional energy flow in terms of electric field ($\mathbf{E}$) and magnetic flux density ($\mathbf{B}$) is defined as:

$$\boldsymbol{S} = \epsilon_0 c_0^2 \boldsymbol{E} \times \boldsymbol{B} \tag{2.30}$$

where S is called Poynting's (Poynting) vector, named after British physicist John Henry Poynting. The flowing energy through an infinitesimally small area of da per second is $\mathbf{S}.\mathbf{n}$,while $\mathbf{n}$ is the unit vector normal to the surface da. One can obtain the total energy flow for an area by integrating over all the surfaces.

The time averaged-Poynting vector carries importance due to practical measurement applications and it is defined as [17]:

$$\langle S \rangle = \frac{1}{2\eta_0} |E_{\mathrm{m}}|^2 \tag{2.31}$$

And intensity (the average rate of energy flow per unit area) is defined base on the previous formula [18]:

$$\textit{Intensity} = \langle S \rangle_{\mathrm{av}} = \epsilon_0 c \left\langle E^2 \right\rangle_{\mathrm{av}} \tag{2.32}$$

The imaginary part of 2.28 is an attenuative term in the direction of wave propagation. The attenuation coefficient is defined as [15]:

$$\alpha \equiv \frac{1}{I} \frac{d}{dz} I \tag{2.33}$$

Here I is the intensity of the electromagnetic radiation and it is proportional to $\mid E \mid^2$, with having 2.29 in mind the intensity can be written as:

$$I(z) = |\mathbf{E}|^2 = I_0 e^{-\alpha z} \tag{2.34}$$

where the I_0 is the intensity of the electromagnetic field at z=0. The extinction coefficient κ is related to attenuation coefficient defined earlier (2.30) and one can write the following:

$$\alpha = \frac{4\pi}{\lambda} \kappa \tag{2.35}$$

The Beer-Lambert law shows the absorption of light and the relation between the attenuation coefficient and the optical pass and it is written as:

$$A = \alpha l \tag{2.36}$$

where l is the optical path of the light. The Beer-Lambert law provides a practical tool for absorption measurements [19].

2.3 Epsilon-near-zero (ENZ) materials

The Drude model describes some metals like silver with enough accuracy. When frequency of oscillations is above ω_p the material behaves like a dielectric and becomes transparent, while below ω_p it stays conductive and reflective as a metal [10].

The real and imaginary parts of the dielectric constant for a 40 nm thick silver are simulated based on the equation (2.14), and the obtained results are presented in Figure 2.1. One can see that around the wavelength of 300 nm, the real part of the primitively goes to zero, while the imaginary part stays positive. This point is considered as epsilon-near-zero (ENZ) wavelength for silver.

Indeed, ENZ materials are defined as any material with a permittivity value near zero, in which the real part of the permittivity transits from a positive value (dielectric state) to negative value (metallic state) at ENZ wavelength [20]. ENZ materials can be either natural or fabricated in the form of metamaterials. Figure 2.2 illustrates some examples of artificial and natural ENZ materials. ENZ metamaterials belong to a group called zero-index-materials that beside ENZs includes mu-near-zero (MNZs) and impedance-matched index-near-zero structures [3].

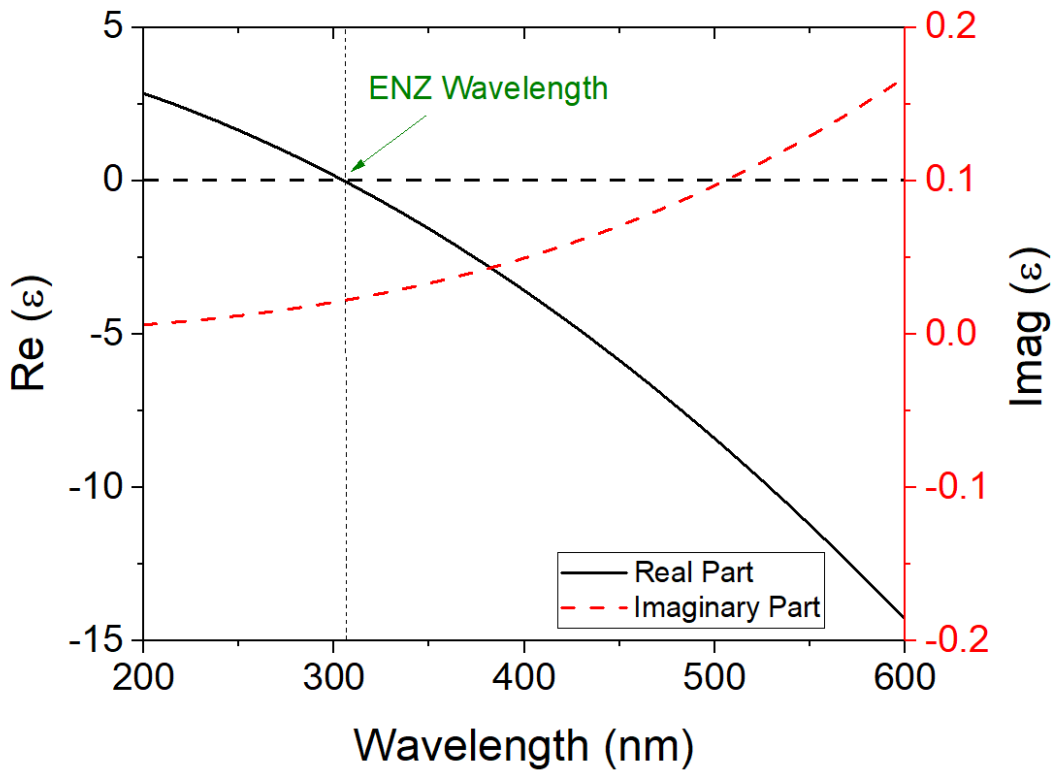

Figure 2.1. *Real and imaginary parts of the dielectric constant for silver according to the Drude free electron model (calculated using MATLAB).*

In a loss-free ENZ material, both real and imaginary parts of the dielectric constant are equal to zero. Using equation 2.18 to 2.24 for such materials, one can expect write the

following equations (2.9) and (2.10) mutually become zero. In other words:

$$\epsilon_{real} = (n)^2 - (\kappa)^2 = 0, \quad \epsilon_{imag} = 2n\kappa = 0 \tag{2.37}$$

However, this kind of material is not found in nature or can not be fabricated due to losses in natural materials. For a lossy ENZ material, although the real part of permittivity reaches zero, the imaginary part stays positive, indicating an attenuation inside the material. One can reckon the real and imaginary parts at the ENZ wavelength and write:

$$\epsilon_{real} = (n)^2 - (\kappa)^2 = 0, \quad \epsilon_{imag} = 2n\kappa = n^2 = \kappa^2 \neq 0 \tag{2.38}$$

In a lossy ENZ material, although the real part is zero, the imaginary part should be minimized, as well. The higher loss values may hinder the practical applications of natural or artificial ENZ materials with a relatively small value of permittivity.

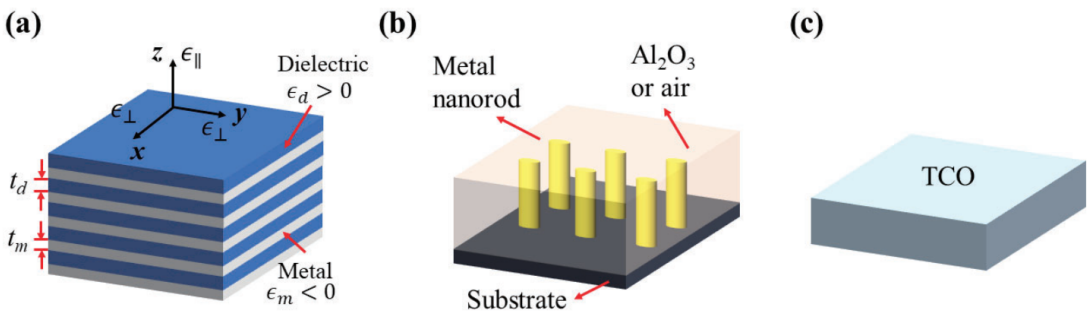

Figure 2.2. *Illustration for artificial and natural ENZ materials.* ***a)*** *Multilayer subwavelength structure,* ***b)*** *nano-rodes inside a dielectric medium,* ***c)*** *transparent conductive oxide (TCO) materials [21].*

2.3.1 The unique optical properties of ENZ materials

ENZ materials show peculiar behavior compared to ordinary materials. The characteristics of ENZ are interconnected and for the sake of simplicity, are separated in this section to draw a more clearer picture.

The phase velocity of an electromagnetic wave is the velocity with which phase fronts propagate inside an optical media [22]. Spatial (λ) and temporal (f) characteristics of an electromagnetic wave, are related to phase velocity (v_p) and can change by traveling through a medium [23]:

$$v_p = f\lambda, \tag{2.39}$$

In other words, the phase velocity (v_p) of a wave inside a medium with permittivity of ϵ is defined as:

$$v_p = \frac{c_0}{\sqrt{\epsilon'}}, \tag{2.40}$$

where c_0 is the speed of light in vacuum. From (2.39) and (2.40) one can get:

$$v_p = \sqrt{\frac{\omega}{k}}, \tag{2.41}$$

where k is the wave vector inside the medium.

Low wavenumber

From equation 2.24, one can see when the permittivity approaches zero. consequently, the wave vector k tends to zero. The relation for spatial wavenumber and frequency is referred as dispersion relation and it is written as [24]:

$$k_i = k_0 \sqrt{\frac{\epsilon_0 \epsilon_m(\omega)}{\epsilon_m(\omega) + \epsilon_0}} \tag{2.42}$$

where k_0 is the free space wavenumber, $\epsilon_m(\omega)$ is the frequency-dependent permittivity for a conductor and k_i is the wavevector along the i axis. As was mentioned earlier, in the ENZ point, the dielectric constant of the material crosses from dielectric to the metallic regime and one can use the 2.38 formula to describe the spatial dispersion of an ENZ medium. For really small values of ϵ_m equation 2.39 shows k_i value that approaches toward zero, meaning the material would acquire a negligible spatial dispersion.

Longer wavelength

The equation (2.39) indicates if the permittivity of a material tends to be near zero; in response, the wavelength can be considerably longer even at higher frequencies. This approves and reaffirms one that the result obtained from equations 2.36 and 2.37, which stated the electromagnetic wave's wavelength stretches inside the ENZ medium. Figure 2.3 illustrates how a wave inside an ENZ medium stretches, as compared to its propagation in a medium with a permittivity far from zero.

Small group velocity

Electromagnetic waves are a superimposition of single waves which can be summed as a wave [26]. It is possible to assign a single velocity to a group of waves or the envelope of the wave-packet as following:

$$v_g = \frac{\partial \omega}{\partial k} \tag{2.43}$$

where v_g is the group velocity, ω is the angular frequency, and k is the wavenumber. By inserting v_p from 2.37 in the above equation, and using the fundamental causality principle, one can attain the dispersion relation for the group velocity of a propagating

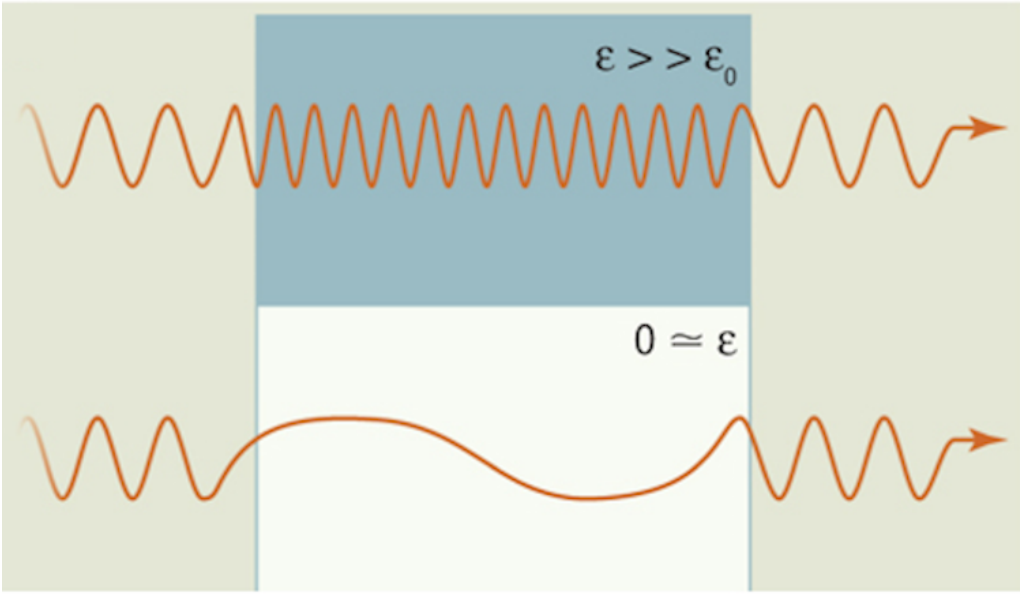

Figure 2.3. *Demonstration of a propagating wave inside an ENZ medium versus a medium with $\epsilon >> \epsilon_0$ [25]. One can spot that the wavelength is stretched inside ENZ metamaterial.*

wave inside medium with the permittivity of $\epsilon = \epsilon' + i\epsilon''$ as following [27]:

$$v_g = c\sqrt{\varepsilon'(\omega)}\left(1 + \frac{2}{\pi}\int_0^\infty \frac{\varepsilon''(\omega_1)}{\left(\omega_1^2 - \omega^2\right)^2}\omega_1^3 d\omega_1\right)^{-1} \tag{2.44}$$

where the integral is the imaginary part of the Fourier transform for the frequency in the form of $a(\omega) = \mathcal{F}[a(t)]$ [28]. To satisfy the stability, the ϵ'' should be a non-negative value. This leads to $V_g \leqslant c\sqrt{\epsilon'(\omega)}$, and near the ENZ frequency ($\omega = \omega_{ENZ}$) the real part of the permittivity $\epsilon'(\omega)$ approaches to zero, resulting in a small group velocity inside the ENZ medium [29, 30].

High phase velocity

The equation (2.40) shows the fact that if the permittivity approaches zero in response, the phase velocity will tend to infinite value [31]. This can be proven through Maxwell equations as well. For a loss-free medium with a $\epsilon = 0$, one can formulate the equations as:

$$\nabla \times H = 0, \quad \nabla \times E = -j\omega\mu_0 H \tag{2.45}$$

where j is the electric current density. In equation 2.42, the magnetic field shows no circulation, and this introduces the constrain $\nabla^2 E = 0$ for the wave. This means that the electromagnetic wave can transmit through an ENZ medium only if it posses an infinitely large phase velocity [32].

Preservation of phase and static behavior

The large value of phase velocity inside an ENZ medium leads to lift spatial constrains for phase conservation. It is worth noting that these effects in a real ENZ material with even a small attenuation are partially preserved, meaning the magnetic curl would have a small but non-zero value. Thus, in reality, phase preserving could not happen in an infinitely long medium [21].

A constant phase has another consequence, which helps to modify the wavefront. An electromagnetic wave entering the ENZ media with an arbitrary incident wavefront will leave the media with conformal waves regarding the exit side of the ENZ media. On account of the fact that waves propagate inside the ENZ medium regardless of shape, one can engineer the exit port of the ENZ media in such a way that can change the phase, as well as, the wavefront of the outcoupling wave.

Low dispersion and wavefront and no-phase variation help engineers to overcome diffraction limits and design far-field imaging devices. A symmetrically curved shape ENZ material can get the light emitted by subwavelength samples and carry the light to the detector. Simultaneously, the media will separate distance between points (increasing resolution), which is similar to magnifying a sample and make it readable for imaging.

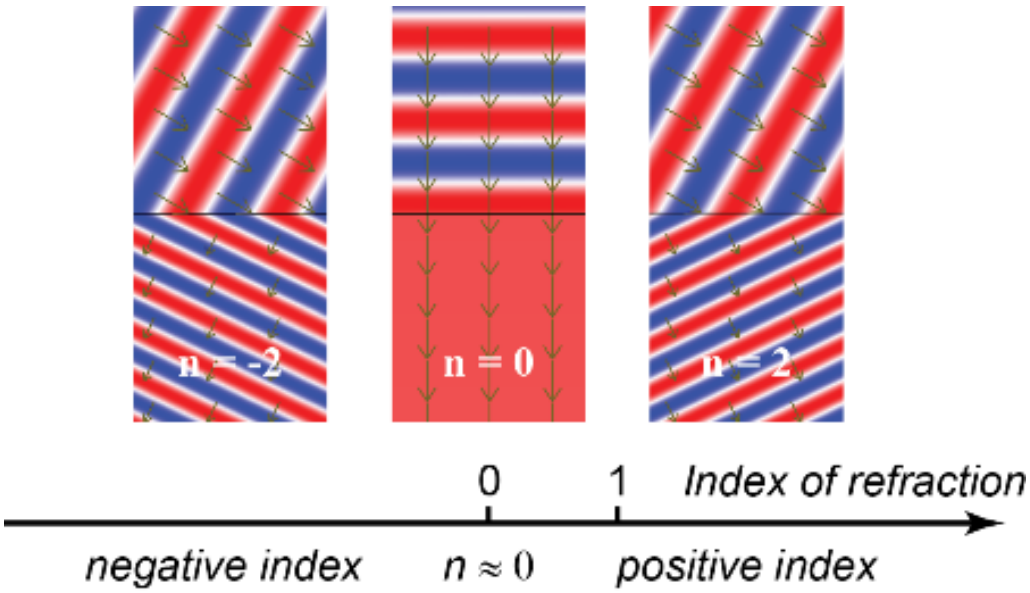

Figure 2.4. *Light-bending behaviors in optical materials that have positive, near-zero, and negative indices of refraction. In an ENZ medium, the electromagnetic fields become homogeneous with a uniform phase distribution and show a static-like behavior [33].*

Directionality

As a result of the impedance mismatch between the ENZ film and the free space, the propagated light through an ENZ material to vacuum can be highly directional [34]. The achieved highly efficient unidirectional transmission is perpendicular to the boundaries in

the interface between the ENZ medium and the free space. The phenomenon of unidirectional transmission from the view of geometric optics can be explained by Snell's law [35]. According to this law, the propagating ray from a material with refractive index n_1, to a material with refractive index n_2 will be refracted, if the incident angle (θ_1) deviates from normal incidence.

$$n_1 \sin\theta_1 = n_2 \sin\theta_2 \tag{2.46}$$

For a propagating beam from an ENZ medium ($n_1 = 0$) to any media with refractive index $n_2 \geqslant 1$, any arbitrary incident angle at the ENZ will impose a perpendicular direction ($\theta_2 = 0$) for the output beam. This will result in a directional beam that leaves the ENZ media.

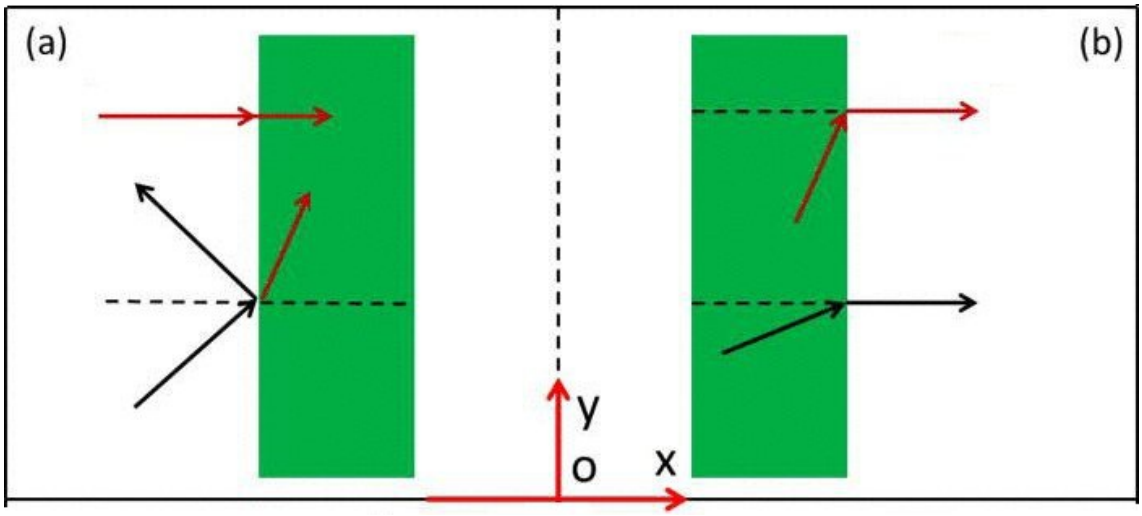

Figure 2.5. *Snell's law and directionality.* ***a)*** *In a normal optical media refraction happens as expected.* ***b)*** *Inside ENZ material all of the rays are refracted to the normal incident.*

Field confinement

The zero value of dielectric constant guarantees local negative polarizability. It means that the phase of scattered fields that are dominated by the dipolar field will be overturned. Boundary conditions between the ENZ and surrounding media impose a high value for the normal component of the electric field. This effect gives rise to many phenomena such as field confinement, supporting highly directive leaky waves and field localization. Figure 2.6 illustrates a rectangular ENZ metamaterial slab in the air environment, which is used to achieve a highly directional filed at the output of the ENZ. The enhanced confined field inside the ENZ medium leaves the exit face of the metamaterial as a highly intense beam [31].

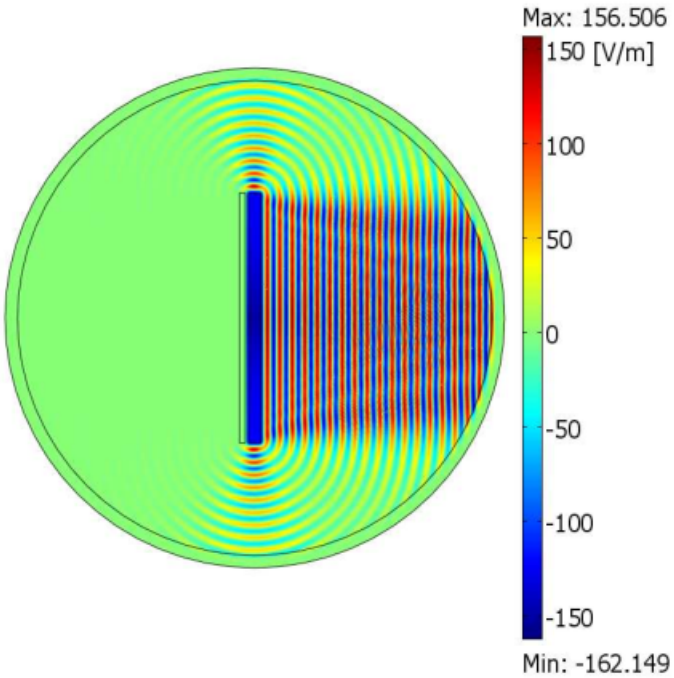

Figure 2.6. *Directionality and field enhancement at the exit face of an ENZ medium [36].*

Internal reflection

From equation 2.24, one can see that the refractive index of an ENZ medium is insignificant in comparison to vacuum ($n = 1$) or any other natural materials ($n > 1$). Such a difference in refractive indices implies a particular phenomenon when a beam enters from a material with a positive refractive index to the ENZ medium. According to Snell's law, the internal reflection at the interface of two media with refractive indices of n_1 and n_2 occurs when the angle of the incidence is equal or more than the critical angle (θ_c) [37].

$$\theta_c = \arcsin\left(n_2/n_1\right) \tag{2.47}$$

Hence, for the ENZ medium ($n_2 = 0$), any incident angle more than zero will be considered as the critical angle and subsequently, the condition for the total internal reflection will be satisfied. This means that due to the significant difference in refractive indices, virtually all of the incident light will be reflected.

Chirality

Chirality happens when an optical object produces a self mirror image that cannot be superimposed on the object itself. In other words, the object produces than asymmetric transmission [38]. Chirality can happen either by the Lorentz reciprocity or the spatial inversion symmetry in the optical material. In an ENZ material, the effect is solely based on anisotropy without reordering to any breaking of reciprocity and chiral symmetries or spatial nonlocal effects [39]. Chiral material are often two- or three-dimensional with

complex chiral structures [40]. However, it is possible to design an ENZ media whose components are achiral, to enhance the optical chirality drastically even in one dimension. Rizza et al., reports a massive enhancement of asymmetric transmission for forward and backward propagation in an ultrathin multilayer hyperbolic ENZ slap [41]. The structure is illuminated with a tilted left-handed and right-handed circular polarized optical waves (Figure 2.7). As a signature of 1D chirality, they show that the designed 1D chiral metamaterials support optical activity, which is the rotation of polarized light clockwise or counter-clockwise direction by a chiral material. Moreover, they prove that this phenomenon undergoes a drastic non-resonant enhancement in the ENZ region of the designed multilayer metamaterial [42].

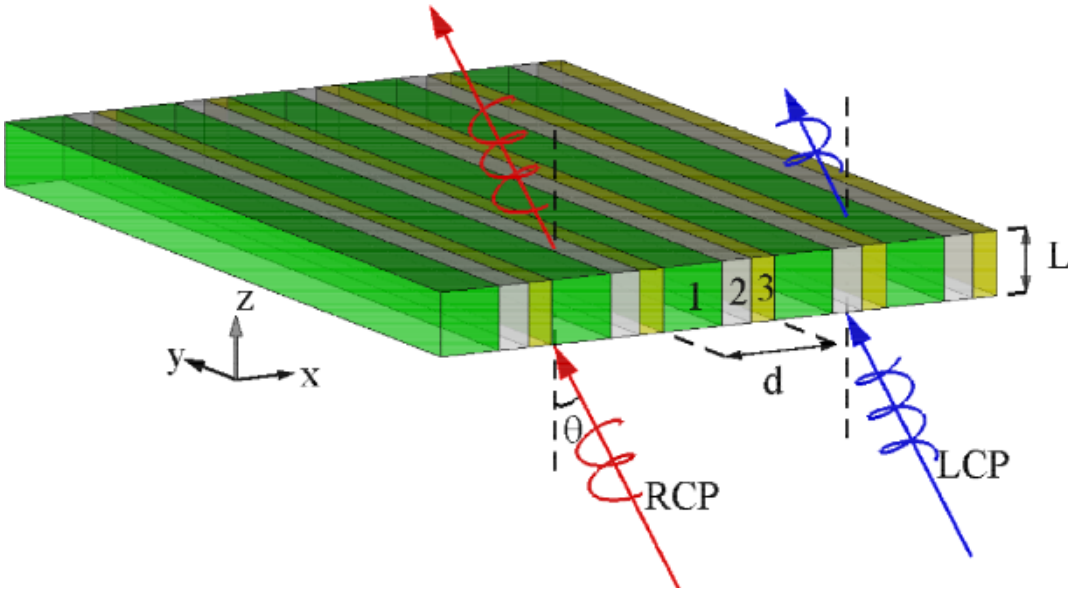

Figure 2.7. *Demonstration of the multilayer metamaterial slab (N = 3 layers) and waves scattering geometry. The propagation amplitudes for the right-handed circular polarized (RCP) and left-handed circular polarized (LCP) plane waves are not equal for $\theta \neq 0$ as an example of 1D chirality. The polarized light rotates by passing through the chiral ENZ metamaterial as a signature of the optical activity [42].*

Nonlinearity enhancement

When a material is irradiated with an intense laser beam, the relationship between the polarization and electric field is different than the equation 2.11, and it becomes nonlinear. If the optical susceptibility is nonlinear, then the material is considered as nonlinear, and higher orders of susceptibility would appear as [43]:

$$P = \varepsilon_0 \left[\chi^{(1)} E + \chi^{(2)} E^2 + \chi^{(3)} E^3 + \chi^{(4)} E^4 + \ldots \right] \tag{2.48}$$

where $\chi^{(1)}$ is the linear optical susceptibility, $\chi^{(i)}$ (i>1) are higher-order nonlinear optical susceptibilities. With a varying field like

$$E = E_0 \cos \omega t \tag{2.49}$$

Equation 2.46 becomes:

$$P = \varepsilon_0 E_0 \left[\chi^{(1)} \cos \omega t + \chi^{(2)} E_0 \cos^2 \omega t + \chi^{(3)} E_0^2 \cos^3 \omega t + \chi^{(1)} E_0^3 \cos \omega t + \ldots \right] \quad (2.50)$$

In equation 2.47, new frequency components appear as higher-order harmonics of the polarization term. One can describe non-linearity as a generation of photons by an intense light source, which is similar to the generation of photons by excitation of electrons in material [44], while these secondary photons interact with the original photons and affect them (Feynman's approach) [45, 46]. In short, light acts as a source of light and interacts with itself [47, 48].

In a non-linear material, the refractive index is written as:

$$n = n_0 + n_2 | \, E \, |^2 \quad (2.51)$$

where n_0 is the refractive index of the medium in the absence of non-linearity, E is the electric field and $n_2 | \, E \, |^2$ is the index change due to the non-linear response where n_2 is called Kerr nonlinearity [49, 50] . ENZ material greatly enhances the nonlinearity in which nonlinear effect is achievable with lower pump intensities [51].The reason can be sought by differentiating equation 2.48, resulting $\delta n \approx \frac{\delta \epsilon}{2n}$. Any minor change in the refractive index will result in a considerable modification in δn and subsequently in the phase velocity. This is the case for an ENZ material, in which at a particular wavelength, its permittivity goes to zero. If one writes the relation between the third-order susceptibility and the permittivity, then it is seen that the nonlinear effect is proportional with $\frac{1}{n^2}$ [52]. This is another perspective to show that for the near-zero values of the refractive index the nonlinear effects can be enhanced drastically [53, 54, 55, 56].

Decoupling of E and H field

In an ENZ medium, by considering μ as zero, the equation 2.42 can be written as:

$$\nabla \times H = 0, \quad \nabla \times E = -j\omega\mu_0 H = 0 \quad (2.52)$$

The previous equation means that the electric and magnetic fields are decoupled. Therefore, in an index-near zero material the electric and magnetic component of the propagating electromagnetic field will spatially distribute statically, while temporally they stay dynamic [57]. Physically speaking, the electromagnetic wave inside this kind of zero-index-materials (ZIMs) behaves as a single spot in space, from an outside observer's view [58].

Super-coupling

Seemingly, the simple phenomena explained earlier for an ENZ material can have a practical application such as super-coupling. Super-coupling inside an ENZ filled waveguide provides the possibility to transmit an electromagnetic wave through a very narrow area with any arbitrary shape, while the oscillating beam spatially propagates statically inside the ENZ waveguide [59]. In this phenomenon, there are three co-occurring events are briefly mentioned here [25]:

1. As the wave passes through the narrower parts of the waveguide, the intensity is enhanced, and this enhancement is inversely proportional to the diameter of the waveguide.
2. A longer wavelength inside the medium means that it has a smaller wavenumber. The smaller wavenumber relatively maintains the uniformity of the phase of the enhanced wave inside narrower parts of the waveguide [60].
3. The enhancement is independent of the ENZ region's shape (whether it is bent or fabricated in a spiral form).

The super-coupling phenomenon is showed in Figure 2.8. As one can see, the electromagnetic field is transferred through a bent arbitrary shape ENZ waveguide without any modification. There are other effects such as second-harmonic generation and also the enhancement of photon density of states inside an ENZ material. All of the mentioned effects make sub-wavelength light manipulation more accessible in an ENZ medium by modifying the relation between frequency and wavelength. In general, for high frequencies, the wavelengths are shortened. However, for ZIM metamaterials, due to relatively low values of permittivity or permeability, the phase velocity of the wave approaches to extremely high values, resulting in long wavelengths at high frequencies.

Perfect absorption

Perfect absorption (PA) has numerous fundamental and industrial applications[61].Total absorption can be utilized and used in practical applications for high-efficiency energy conversion. It is possible to design PA using ENZ metamaterials [62]. In transparent conductive oxides(TCOs), the dielectric constants are tuned by changing doping densities. Based on the doping density, ENZ wavelength can be defined in a certain spectral region so-called as the ENZ region. As a result of the transition from dielectric to the metallic state, in the spectral region beyond the ENZ wavelength, the subwavelength TCO films can present plasmonic properties. The perpendicular component of the electric field (E_z) in a plasmonic subwavelength thin film becomes intensely enhanced and this can lead to extensive light absorption in the film [63]. The maximum absorption for a free-standing thin film is 50% , but it is possible to increase it up to 100% (i.e. PA) under certain conditions [64]. One example is if a subwavelength plasmonic thin film is coated over a metallic substrate or attenuated total reflector (ATR) is used, the destructive interference for the

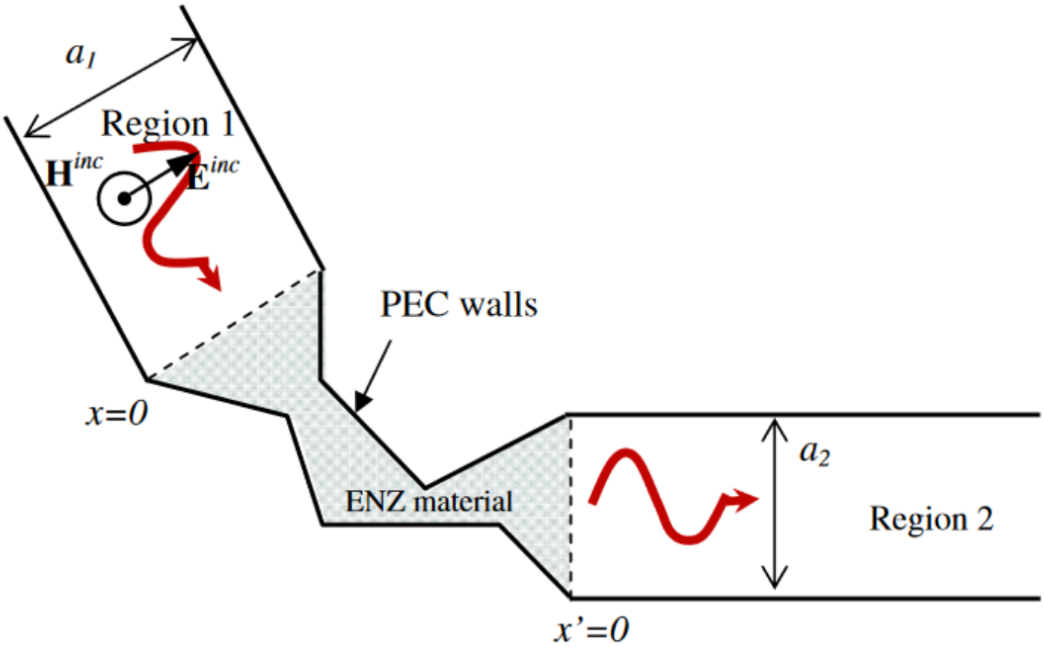

Figure 2.8. *A two dimensional arbitrary shaped ENZ-filled waveguide (grey part is ENZ) carrying an electromagnetic wave. It is seen that unlike regular optical materials the light is traveling through the bent narrow parts because of super-coupling phenomenon [25].*

reflected light in the transverse magnetic mode is written as [65]:

$$\frac{2d\pi}{\lambda} = \frac{\mathrm{Im}(\varepsilon)}{n_0^3 \sin\theta_0 \tan\theta_0} \quad (\text{ when } \mathrm{Re}[\varepsilon] \to 0) \tag{2.53}$$

While λ is attributed to the wavelength of the incident light, θ_0 is the incidence angle, n_0 is the refractive index of the incidence medium, d is the film thickness and ϵ is the dielectric constant of the thin film. Transmission, in this case is really low because of the opaque substrate or propagation of the evanescent wave in ATR mode, this means only the interference of the reflected light should be considered. Unlike other methods, this PA is achieved using an ultra-thin ENZ flat film layer with a small optical loss. However, this formula can be satisfied in a specific wavelength, which limits the applications.

2.3.2 Transparent Conductive Oxides (TCOs)

Metal oxides like MgO are optically transparent in the visible region, but they are insulators. On the other hand, semiconductors such as Si and Ge are only transparent in the infrared region. The need for both conducting and transparent material in the visible region highlights the role of transparent conductive oxides (TCO) in the electronics [66].

TCOs, as a type of electrical conducting thin films, are used in various electronic devices, namely LCDs, OLEDs, solar cells and touch screens [68]. The chemical composition of TCO is composed of a metal part with two or several metals and a nonmetal part of oxygen. The metal part of TCO makes a compound semiconductor and there is a

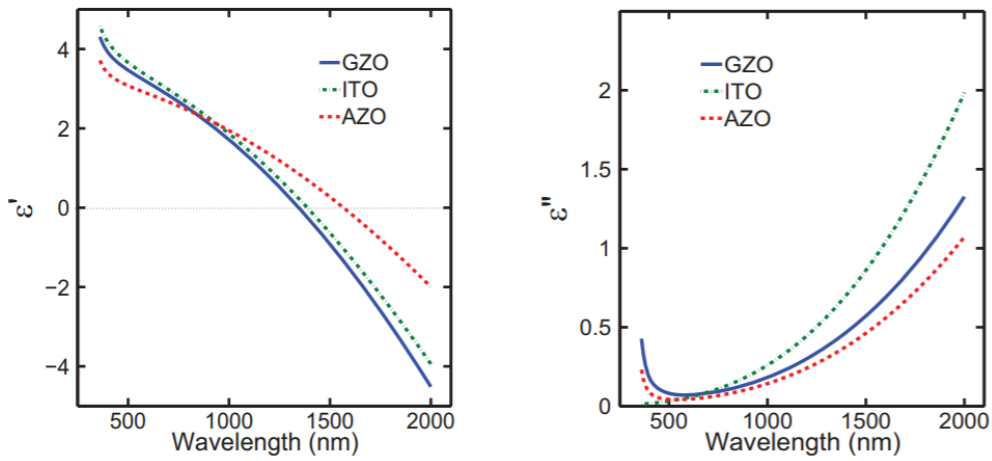

Figure 2.9. *Comparison of permittivity for three common TCO materials with ENZ wavelength around 1500 nm. The ϵ'' can greatly affect ENZ properties and it depends on the material and fabrication process [67].*

possibility of adding a dopant made of metal, metalloids, or nonmetals. Doping TCOs structure opens the possibility to adjust optoelectrical properties of TCOs [69]. Two types of TCOs are n-type, and p-type delafossite TCOs [69]. In this work, only n-type would be discussed, because ITO is an n-type TCO and it is used as an enhancing layer in our design [69]. The first TCO ever made dates back to 1907, when a thin film of Cadmium oxide (CdO) created by thermal oxidizing of a vacuum sputtered film of cadmium. CdO is not a commonly used material, because of the toxic nature of the cadmium [70]. One of the first uses for TCO is known for SnO_2 used as an anti-static layer. Tin oxide (TO) was also utilized in the aviation industry in airplanes windshields, as a transparent heater film in a method called pulse interfacial defrosting. In this method, transient heat fluxes of $\approx$50 $\frac{W}{cm^2}$ is transferred to the TCO layer to melt the ice over windows. However, nowadays TO is replaced with Indium Tin Oxide (ITO) [70, 71].

ITO is composed of 90% wt of Indium oxide (In_2O_3) and 10%wt of Tin oxide (SnO_2). There are several methods to deposit ITO depending on needs such as composition accuracy, substrate's thermal stability and etc. For instance, if an organic substrate is used, the coating process is done using plasma ion-assisted evaporation. This method would avoid higher temperatures that can destroy the substrate and the whole process is done in temperatures below 100° C [72]. With a sol-gel solution method, an ITO thin film can achieve an electrical resistivity of $4 \times 10^{-3}\ \Omega.m$ and transmittance of 90% [73, 74]. Methods such as dip-coating with commercial ITO nanopowder-ethanol dispersion can obtain a transmittance of 95% and resistivity of $5.10 \times 10^{-3}\ \Omega.m$ [75]. One can use a post-annealing technique to change optical transparency, conductivity grain size, or surface roughness of an ITO for different purposes, such as modifying the ENZ region of the material. It is worth reminding that after ENZ region, the material starts to behave like a metal, instead of a dielectric [76].

There are two mechanisms responsible for the absorption of photons outside the visible region. In a longer wavelength, in materials such as Ge or Si, the absorption is caused by the lattice vibrations. In shorter wavelengths, in materials such as thin metal films, due to a large bandgap between the valance band and conduction band, light is absorbed in the ultraviolet region. However, a material like ITO is both conductive and transparent between these two spectral regions [66].

ITO has limitations of use due to a shortage of supply. However, for a TCO like aluminum-doped zinc oxide (AZO) supply problem is solved. Another advantage of AZO is that it can be produced using cheaper substitute material, by sputtering ZnAl over a substrate for commercial productions [77]. A disadvantage of AZO is the etching process, which can not be done with enough accuracy. The reason can be sought in sensitivity of AZO to acids which result in over-etching during the fabrication process [78].Another common TCO is Gallium-doped Zinc Oxide (GZO), which can be dopped higher with a higher density than other TCOs. The optical properties of GZO can highly vary depending on the concentration of the dopant and this variation does not follow a simple dependence rule. This drawback creates difficulties and complexity in the design of GZO based metamaterials [79].

In principle, TCOs as low-loss plasmonic materials in the near-infrared (NIR) spectral range, are promising candidates to realize fascinating applications such as metamaterial-inspired nanocircuits and integrate them with silicon-based optoelectronic applications [80]. In particular, the ENZ feature of these materials opens up the avenue for exploiting their extraordinary properties to build up low-loss ENZ metamaterials operating in the NIR region. In Figure 2.9, the measured real and imaginary parts of the permittivity based on the ellipsometry method for three TCOs, including AZO, GZO and ITO, are presented. One can see that all three mentioned TCOs are presenting ENZ features around 1500 nm. The imaginary part of the permittivity can be optimized depending on the fabrication process and material type, as it was mentioned earlier [67].

2.3.3 Artificial ENZ metamaterials

Using a proper composition of metallic and dielectric materials, one can design a sub-wavelength structure with ENZ behavior in the visible range. Such structures are known as hyperbolic metamaterials (HMMs), which exhibit effective permittivities with different signs in the parallel and perpendicular orientation of the crystal. By considering the presence of non-magnetic materials in the structure of an HMM, permeability can be considered as a unit tensor in the shape of a 3x3 diagonal matrix.

$$\epsilon = \begin{bmatrix} \epsilon_{xx} & 0 & 0 \\ 0 & \epsilon_{yy} & 0 \\ 0 & 0 & \epsilon_{zz} \end{bmatrix} \tag{2.54}$$

Generally, these three components are frequency-dependent (dispersive), which are oriented along so-called principal axes of the crystal. A crystal is isotropic when all three diagonal elements are the same. ITO, as a composite structure, is a good example of an isotropic crystal, in which the linear dispersion and isotropic behavior of propagating waves imply a spherical isofrequency surface. A crystal is termed as biaxial when none of these three elements are equal to each other. It becomes uniaxial when two of the components, for example, in the x and y direction are the same, but different from the other one (in the z-direction). In a uniaxial medium, for TM polarized (extraordinary) waves, the spherical isofrequency surface changes to the elliptical as the following equation.

$$\frac{k_x^2 + k_y^2}{\varepsilon_{zz}} + \frac{k_z^2}{\varepsilon_{xx}} = \frac{\omega^2}{c^2} \tag{2.55}$$

It is worth noting that waves polarized in the xy plane are called ordinary, or TE, while the waves polarized in a plane containing the optical axis of the crystal are called as extraordinary or TM. In the above equation k_x, k_y, k_z are the wave-vectors of the propagating wave in the crystal. The equal in-plane isotropic components ($\epsilon_{xx}, \epsilon_{yy}$) are the parallel components ($\epsilon_{||}$) and out of plane component (ϵ_{zz}) is considered as the perpendicular component ($\epsilon_{\perp}$). Thus, in vacuum, the anisotropic feature of the crystal distorts the spherical isofrequency surface to an ellipsoid one. The situation changes significantly if one assumes an extreme anisotropy, which means that one of the parallel or perpendicular permittivity components is negative. Mathematically, a material with such an optical behavior is termed indefinite, since its permittivity tensor represents an indefinite non-degenerate quadratic form. In such a case, according to the effective medium theory, the crystal produces a hyperboloidal isofrequency surface with an infinite volume. Consequently, such medium possesses a broadband singularity in the photonic density of states in a broad spectral range [81].

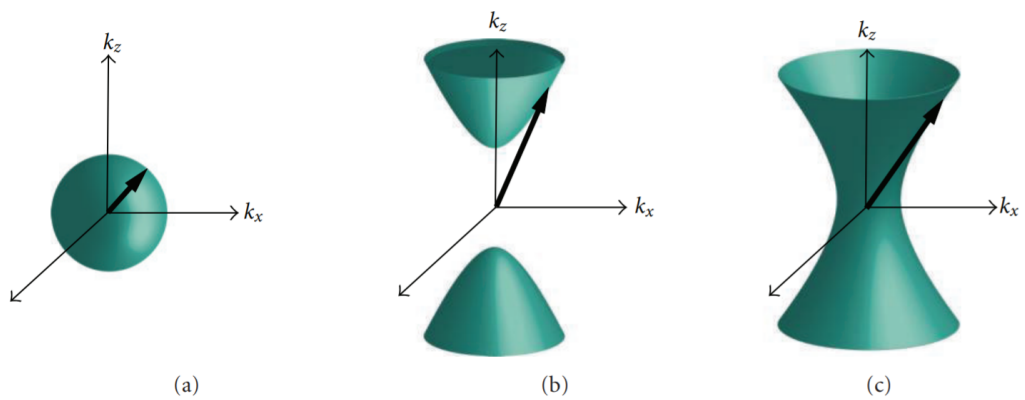

Figure 2.10. *k-space topology.* ***a)*** *For a conventional isotropic dielectric, the isofrequency surface is a sphere. Only waves with limited k-vectors are supported.* ***b)*** *Type I HMM ($\epsilon_{||} > 0, \epsilon_{\perp} < 0$).* ***c)*** *Type II HMM ($\epsilon_{||} < 0, \epsilon_{\perp} > 0$). The black arrows represent the wavevectors supported by the material [81].*

In addition, the unbounded isofrequency surface of a hyperbolic medium creates the pos-

sibility for keeping a propagating nature for the waves with arbitrarily large wavevectors, while due to the bounded isofrequency surface of an isotropic materials they become evanescent and decay exponentially. Moreover, the open form of the isofrequency surface in a hyperbolic medium supports propagating waves with infinitely large wave-vectors, so-called as high-k wave-vectors or high-k modes [81].

One can classify the hyperbolic metamaterials in two categories of Type I and Type II. In a particular spectral range, a structure with positive parallel effective permittivity ($\epsilon_{xx} = \epsilon_{yy} > 0$) and negative perpendicular effective permittivity ($\epsilon_{zz} < 0$) is called Type I HMM. In this case, the isofrequency surface is a double-sheeted hyperboloid, and the metamaterial supports both low-k and high-k wave-vectors (Figure 2.10 (a)). If, after a particular wavelength, the effective parallel components of the dielectric tensor get negative ($\epsilon_{xx} = \epsilon_{yy} < 0$) and perpendicular effective permittivity ($\epsilon_{zz} > 0$) stays positive, the structure is referred as Type II HMM. The isofrequency surface of such material is a single-sheeted hyperboloid and waves with parallel wavevectors above kmin are supported, while below k_min are reflected (Figure 2.10 (b)). The presented subwavelength metal-dielectric multilayer structure in Figure 2.2 (a) behaves as a Type II HMM and the subwavelength parallel metallic rods in dielectric host medium in Figure 2.2 (b) acts as a Type I HMM in the visible spectral range.

Out of the hyperbolic region, both the effective parallel and perpendicular components of the dielectric tensor stay positive. In this case, the artificial subwavelength structure behaves as a dielectric, and it implies an elliptical isofrequency surface in all crystal's orientation. This means that after a particular wavelength, as the effective parallel and perpendicular permittivities take opposite signs ($\epsilon_{||}\epsilon_{\perp} < 0$), the ellipsoid isofrequency surface of the structure distorts the hyperbolic one. The discussed particular wavelength is considered as the ENZ wavelength (λ_{ENZ}), and therefore, the spectral region between the elliptical and hyperbolic ones is called ENZ region, in which the value of the parallel or perpendicular effective permittivity (depending to the type of the HMM) stays close to zero.

For a multilayer structure, after λ_{ENZ}, the effective parallel permittivity goes from positive to negative values, while the medium in z-direction shows continuously the dielectric behavior (perpendicular permittivity stays positive in visible spectral range). Subsequently, for this particular orientation, the structure shows a metallic behavior below λ_{ENZ} and a dielectric property above it. This means that the nanostructure will be mostly transmissive below λ_{ENZ}, while it becomes mostly reflective above this wavelength. Figure 2.11 shows an example of multilayer structure, composed of 16 nm of Au and 32 nm of TiO2 is fabricated on fused silica (SiO2) substrate, which shows a transition from metallic to a dielectric state above λ_{ENZ} located at 605 nm, as the effective parallel permittivity goes from positive to negative value after this wavelength In this Figure, the simulated and measured reflectance and transmittance spectra of the designed multilayer HMM are presented, as well.

Based on Maxwell-Garnet approach and Bruggeman formalisms, "extended effective

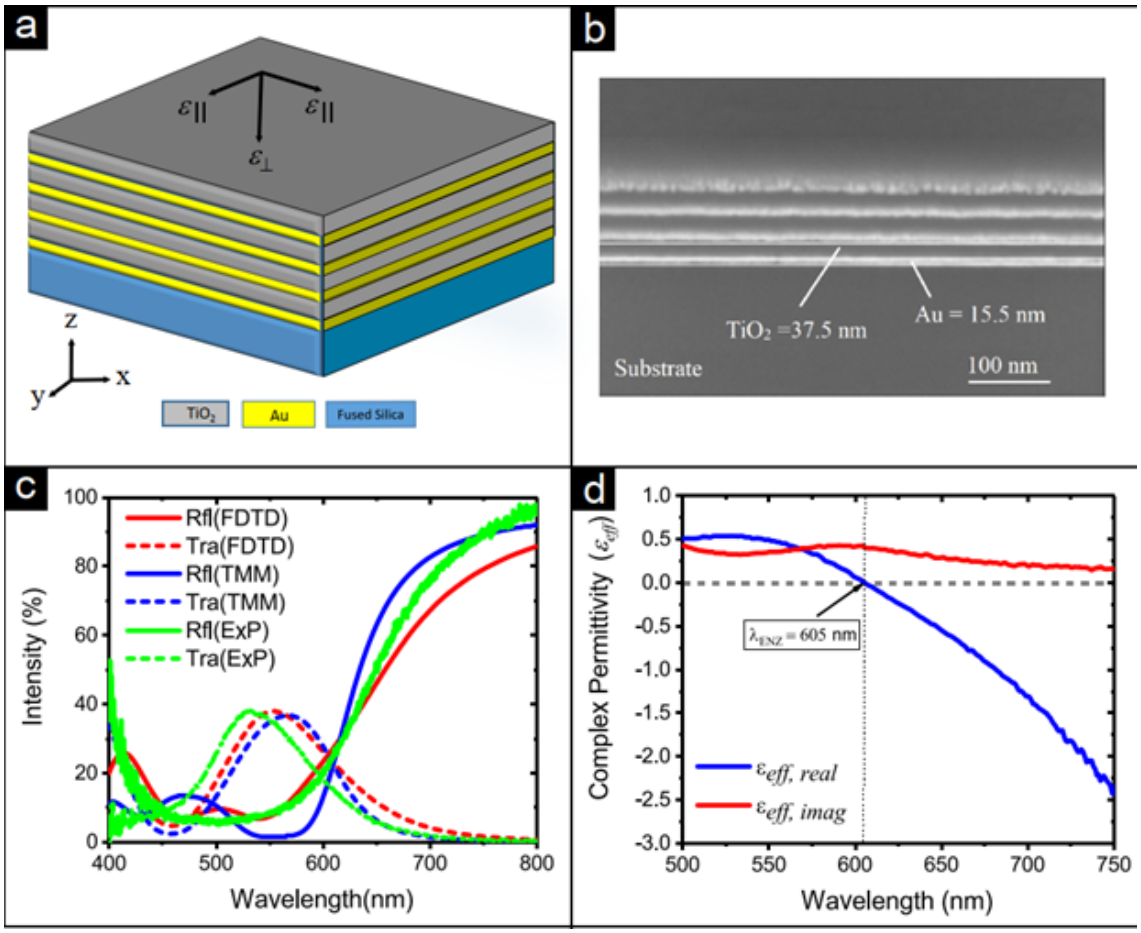

Figure 2.11. ***a)*** *Schematic of a layered metal-dielectric structure with sub-wavelength thicknesses.* ***b)*** *The cross-sectional SEM image of the fabricated multilayer metamaterial.* ***c)*** *The simulated and experimentally acquired reflectance (solid lines) and transmittance (dashed lines) of the metamaterial.* ***d)*** *The real and imaginary parts of the effective parallel complex permittivity with an ENZ wavelength at 605 nm [82].*

medium theory" is applicable for a low loss structure with sub-wavelength unit cells (typically 20-70 nm), operating in the visible spectral range [83]. Accordingly, the dielectric constants of the designed multilayer structure consisted of metal and dielectric layers with subwavelength thicknesses is defined as effective values in parallel and perpendicular directions based on effective medium theory [84]. This theory provides a way to express the effective parallel and perpendicular permittivities for a multilayer HMM structure when the permittivities of each layer are known. This is crucial for designing a structure showing desired behaviour on chosen wavelengths. One can drive effective parallel and perpendicular permittivities of the multilayer nanostructure, by considering the first Maxwell equation and appropriate boundary conditions on it. In addition, in these calculations, two points need to be considered: I) The tangential component of the electric field ($\vec{E}$) must be continuous across an interface as we go from one medium to another. II) The normal component of the electric displacement vector ($\vec{D}$) at metal-dielectric interfaces must be continuous.

To derive the permittivities, metal fill fraction ρ needs to be defined as

$$\rho = \frac{d_m}{d_m + d_d}, \tag{2.56}$$

where d_m and d_d are the total summed thicknesses of metal and dielectric layers. First, effective parallel permittivity is derived. From the definition of permittivity, it is known that

$$\vec{D} = \vec{\epsilon}_{eff}\vec{E}, \tag{2.57}$$

where $\vec{D}$ is the electric displacement in the medium caused by an electric field $\vec{E}$ and $\vec{\epsilon}_{eff}$ is the effective permittivity of the medium. The tangential component of the electric field remains continuous across an interface, thus

$$E_m^{\parallel} = E_d^{\parallel} = E^{\parallel}, \tag{2.58}$$

where $E_m^{\parallel}$, $E_d^{\parallel}$ and $E^{\parallel}$ are the parallel component of the electric field in metal layers, dielectric layers and the metamaterial. The overall electric displacement across the material is found by averaging the contributions of both metal and dielectric layers:

$$D^{\parallel} = \rho D_m^{\parallel} + (1-\rho)D_d^{\parallel}, \tag{2.59}$$

where $D_m^{\parallel}$, $D_d^{\parallel}$ and $D^{\parallel}$ are the displacements in metal layers, dielectric layers and the metamaterial.

Combining equations 2.57, 2.58 and 2.59 the effective parallel permittivity of the metamaterial is found to be

$$\epsilon_{\parallel} = \rho\epsilon_m + (1-\rho)\epsilon_d. \tag{2.60}$$

By substituting ρ from 2.53 in 2.57, the effective parallel permittivity can be written as follows

$$\epsilon_{\parallel} = \frac{d_m\epsilon_m + d_d\epsilon_d}{d_m + d_d}. \tag{2.61}$$

Next, the effective perpendicular permittivity will be derived. At an interface, the normal component of the electric displacement vector stays constant

$$D_m^{\perp} = D_d^{\perp} = D^{\perp}, \tag{2.62}$$

where $D_m^{\perp}, D_d^{\perp}$ and $D^{\perp}$ are the electric displacement in the metal layers, the dielectric layers and the metamaterial. Based on the superposition principle, the total electric field in the metamaterial is the sum of the field components in the metal and dielectric layers such that

$$E^{\perp} = \rho E_m^{\perp} + (1-\rho)E_d^{\perp}, \tag{2.63}$$

where $E_m^{\perp}$, $E_d^{\perp}$ and $E^{\perp}$ are the perpendicular components of the electric field in metal layers, dielectric layers and the metamaterial. Combining equations 2.57, 2.62 and 2.63

the effective perpendicular permittivity of the metamaterial is discovered to be

$$\epsilon_{\perp} = \frac{\epsilon_m \epsilon_d}{\rho \epsilon_d + (1-\rho)\epsilon_m}. \tag{2.64}$$

By substituting ρ from 2.56 in the above equation, we can write

$$\epsilon_{\perp} = \frac{(\epsilon_m \epsilon_d)(d_d + d_m)}{d_m \epsilon_d + d_d \epsilon_m} \tag{2.65}$$

By considering the opposite sign for $\epsilon_{\parallel}$ and $\epsilon_{\perp}$, at a certain spectral range above the λ_{ENZ}, the multilayer structure starts to behave as HMM.

2.4 Optical behavior of subwavelength apertures

2.4.1 Single aperture

A circular aperture in an infinitely thin perfect electrical conductor (PEC), which is shown in Figure 2.12 has been studied first by Bethe [1]. As one can see, the incident plane wave propagates toward a circular hole with a radius of r. The transmitted light is diffracted with a circular pattern, where the θ is the angle between the incident light rays (or normal line to the screen) and the direction of the emitted light.

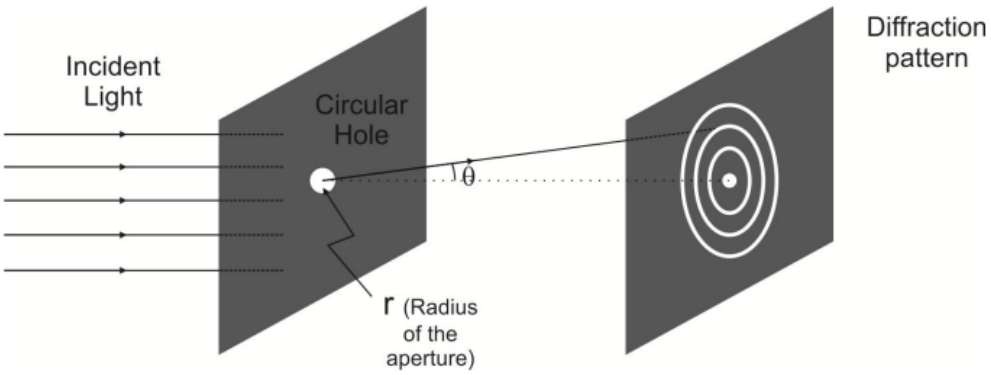

Figure 2.12. *Transmission of light through a circular aperture of radius r in an infinitely thin opaque plate. The circularly diffracted pattern is formed on the projection screen [85].*

When r is considerably larger than the wavelength λ_0, one can use Huygens-Fresnel principle. The mathematical calculation of diffraction obeys the Kirchhoff scalar theory of light diffraction [86]. However, the subwavelength apertures demonstrate different behavior. While r< λ_0, the near field is the dominant factor in the transmission of the incident light [87]. Bethe and Bouwkamp reached an analytical solution for transmission of light through a subwavelength hole in the PEC screen. They calculated the transmittance by assuming the intensity of incident light (I_{inc}) is constant over the area of the aperture [1, 86].

Other approaches such as Maier's theory proposes that the aperture is assumed to be a magnetic dipole which is placed in the plane of the hole. According to Maier's theory [2], the transmission coefficient is calculated as follows:

$$\mathrm{T} = \frac{64}{27\pi^2}(\mathrm{k.r})^4 \propto \left(\frac{\mathrm{r}}{\lambda_0}\right)^4 \tag{2.66}$$

This formula is written for a plane incident wave with a wavenumber of k. The ratio of the transmitted power (T) to the incident power in the hole area of (I_0) is negligible. This ratio is proportional to the fourth of the linear electrical dimension of the aperture [88]. This calculated transmission for the mentioned subwavelength aperture ($r << \lambda_0$) is much smaller than the result obtained by Kirchhoff's scalar theory ($(\frac{r}{\lambda_0})^2$). The $T \propto {\lambda_0}^{-4}$ factor agrees with Rayleigh scattering for small objects. Equation 2.66 deals with a normal light with a TEM (both transverse electric and transverse magnetic) polarization. When radiation propagation direction is not normal to the screen, another electric dipole in the perpendicular direction is needed for explaining the transmission. For a TM mode more radiation is transmitted as compared to TE mode [1]. Subsequently, the transmission of the TM mode incident light is investigated more thoroughly in this thesis.

Young's double-slit experiment demonstrates that the interference of two single slits can result in an interference pattern. This pattern shows dark and light bands that are resulted from destructive and constructive interference respectably. These bands are formed when a coherent light passes through two neighboring single slits, and due to length difference in optical paths of two split beams, an interference pattern is created. When the number of slits increases, instead of these bands (fringes), dark spots with zero intensity will be formed. These spots have undefined phases rather than a single determined phase; alternatively, it can be expressed that these spots have infinite undetermined phases [89]. These spots are known as optical vortices (points of phase singularities).

Figure 2.13 (a) and (b) show 3D and 2D views of a saddle shape formation of an electromagnetic field's Poynting vectors, respectively. Figure 2.13 (c) depicts the power flow of the Poynting vectors, which is the equivalent representation of the phase for the same field. The center of the represented phase and Poynting vectors fields respectively in b and c panels are considered the point of singularity [90].

Schouten et al. reported that subwavelength slits create several phase singularities for the electromagnetic light even before entering the slit. As it is discussed in later, this depends on the field formation due to Propagating surface plasmons (PSPs), Localized surface plasmons (LSPs) in cavities, and dielectric material near the slit entrance [90]. Furthermore, it is shown that any changes in slit size can create or annihilate new phase singularities. This phenomena is observed for transmittance enhancement [91] and transmittance frustration [92]. An electromagnetic wave's wavefront can be changed in different forms [93] in which with proper phase engineering, one could obtain EOT of the light in subwavelength structures [94, 95].

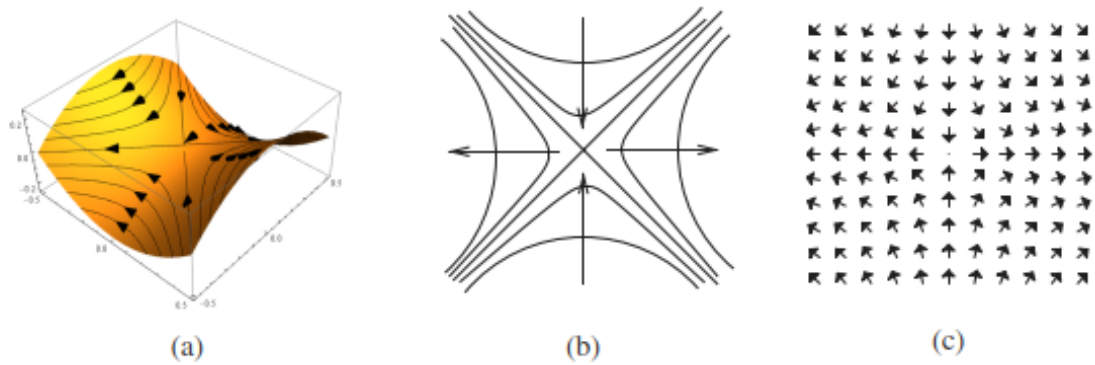

Figure 2.13. *Phase saddle* ***a)*** *3D view and* ***b)*** *2D view of the visualizing contour for points with the same phase.* ***c)*** *Power flow saddle [90].*

2.4.2 Transmission through a single sub-wavelength slit

A single subwavelength slit is more complex than a circular aperture. However, there are many reasons to investigate a single slit more extensively. A single subwavelength slit is considered as a single defect with a directional beam, which acts as an array of optical launchers. Laluet et al [95]. showed a semi-infinite slit which, leads to a directional transmission of the incident light. They also proved that divergence of this directional transmission could be tuned by changing the illumination conditions such as focus waist and polarization state of the incident beam and the type of the light source (laser or broadband beam) [95, 96] .

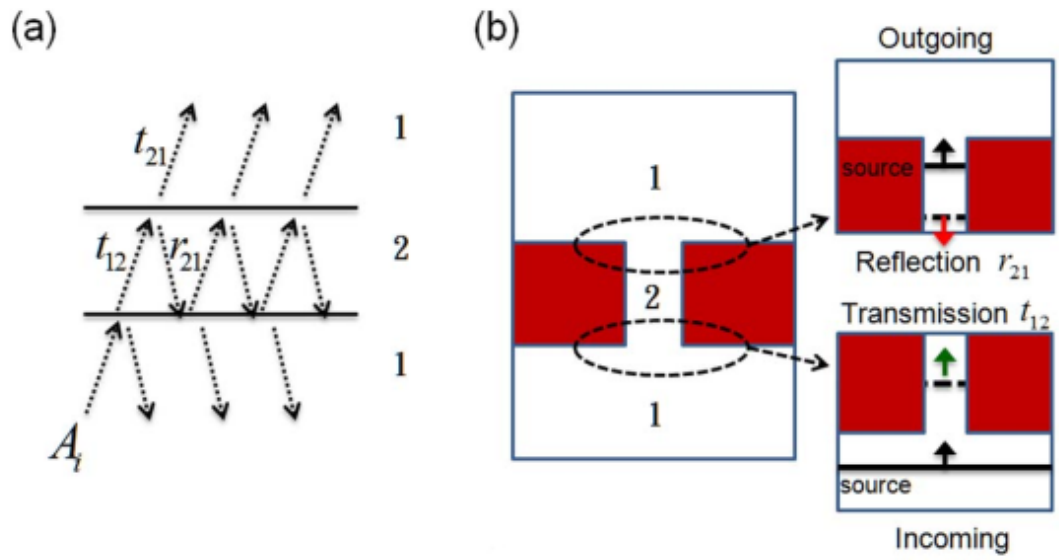

Figure 2.14. ***a)*** *Fabry-Perot model or etalon as an optical cavity made from two parallel reflecting surfaces. Optical waves can pass through the optical cavity only when they are in resonance with it.* ***b)*** *Two incoming and outgoing interfaces of a single slit. The insets represent the transmission component through the incoming surface and the reflection component from the outgoing surface of the slit which acts as a semi-waveguide [97].*

For a single subwavelength slit, it is shown that light transmission has a strong depen-

dence on film thickness. If the film thickness is fixed [98]. As it was mentioned earlier, the polarization of incident light affects the transmittance through a subwavelength slit. For a slit with a width smaller than half of the wavelength that is illuminated with a TE polarized light (an electric field parallel to the slit's long axis), if the thickness of the slit increases, then it results in a zero transmission of the light. The first waveguide mode (considering the slit as a waveguide) in a perfect electric conductor (PEC) has a cut-off width of $W_{cut-off} = \lambda/2$. For a TM polarized light that the electrical field is perpendicular to the sides of the walls (to the slit's long axis), the electric field induces surface charges on the slit walls, which results in the funneling of the light through the slit. The slit affects the energy flow through and around itself and diffracts the wave with different orientations. This results in a cylindrical wave near the incident zone [99].

2.4.3 Hybridization of plasmonic modes in subwavelength apertures

Surface plasmons are described as coherent oscillations of free electrons at the interface of metal and dielectric in resonance with the electric component of the incident electromagnetic wave [100]. Surface plasmons can be classified into two categories: propagating surface plasmons (PSPs) and localized surface plasmons (LSPs) [101]. PSPs are electromagnetic waves that propagate along with the interface between a metal and dielectric. The electromagnetic field of PSPs are localized perpendicular to the surface of the metal and decay exponentially with the distance from the interface. It is possible to excite PSPs by photons with the same frequency and momentum of oscillating plasmons. The PSPs attenuate quickly due to the absorption which happens inside the metal. The evanescent normal component of a PSP drops exponentially with distance. Since the average Poynting vector for this evanescent field is zero, there would be no actual energy flow in the normal direction to metal surface [102].

LSPs are defined as collective oscillations of free electrons localized at metallic surfaces. LSPs lead to a confined and substantially enhanced field compared to the intensity of the incident excitation field. LSP resonances occur solely in structures that their size is considerably smaller than the wavelength of the incident light. LSPs are not propagating waves like PSPs; they can be used as plasmonic sub-diffraction electromagnetic waveguides, which can be utilized in building broadband and fast nanocircuits and devices [103].

Plasmon resonances of complex geometrical metallic nanostructures can be clarified by means of the plasmon hybridization model [105]. According to this theory, one can interpret the plasmonic behavior of a composite system, which is a blend of several interacting surface plasmons, as the collective interactions of plasmons related to simpler geometries. This approach is analogous to the hybridization of molecular orbits in molecular orbital theory [106]. In thin films, grooves or apertures can behave as a cavity for the surface modes, therefore reduces their group velocity and dramatically increases the field

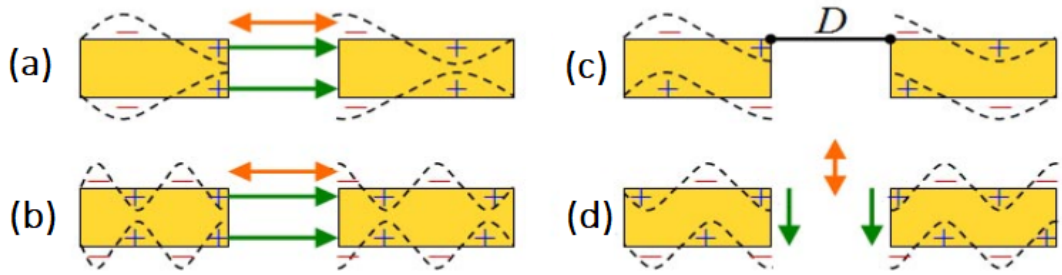

Figure 2.15. *optimal coupling of* ***a)*** *a bonding mode film plasmon mode and* ***b)*** *a higher-order bonding mode film plasmon mode with light of parallel polarization.* ***c)*** *No coupling between any anti-bonding film plasmon mode and light of parallel polarization.* ***d)*** *Optimal coupling between an anti-bonding film plasmon mode and light of perpendicular polarization. Orange arrows represent the polarization direction of the incident light, and green arrows indicate the dipole moments resulting from the plasmon-induced charges on the surfaces of the hole [104].*

confinement at the interface region [107]. The plasmon hybridization approach demonstrates that the dispersion relations of the plasmon modes of an opening (cavity) on thin metallic films are corresponding to those of a continuous film. It is worth noting that in a thin metallic film, one can observe bonding (symmetric) and anti-bonding (asymmetric) plasmon modes. For an opening (cavity) on a metallic thin film, the film plasmons can induce charges along the walls of the hole. These film plasmons, exposed by the presence of the hole, become optically active and can be directly excited in contrast to the surface plasmon waves of a continuous film, which require evanescent excitation. Plasmon modes of corresponding spatial wavelengths can thus induce a dipole moment across the opening (cavity) [101].

Figure 2.15 (a) and (b) show optimal coupling between bonding (symmetric) modes and an incident light with parallel wave polarization. The figure demonstrates the physical mechanism responsible for the excitation of the cavity plasmon resonance (LSP). In the dipole approximation, the coupling of light with surface plasmons is proportional to the square of the dipole moment of the plasmons. For this reason, light polarized parallel to the surface can couple only to bonding film plasmons. As is evident in panel (c), there is no coupling between the anti-bonding (asymmetric) mode with this state of the polarization. On the other hand, perpendicularly polarized light can couple to anti-bonding plasmons (Figure 2.15 (d)). On a continuous metallic surface, the plasmons possess no dipole moment. However, in the presence of a cavity, the film plasmons can obtain a dipole moment due to the localized surface charges (LSP modes) induced along the walls of the cavity [104]. The symmetric and asymmetric film plasmons are responsible for constituting the cavity resonance, rather than a localized hole-induced plasmon resonance. Since the energies of thin-film plasmons also depend on the thickness of the film, the energy of the cavity mode will also depend on film thickness.

In thin films, a decrease in the film thickness can lead to increase in the electrostatic inter-

action between the surface charges on the opposite sides of the hole. Greater wavevector surface plasmons can also induce localized dipole moments across a subwavelength opening on a metal surface [104].

2.4.4 Extraordinary Optical Transmission (EOT)

One of the most attractive phenomena in photonics is the extraordinary optical transmission (EOT), which occurs when a periodic array or optical subwavelength opening transmits extraordinary intensity of an incident light through a metal film [108]. The EOT happens when the intensity of the transmitted beam through a sub-wavelength aperture is highly enhanced by engineering the physics of the structure, while the geometry or size of the aperture is kept constant. Therefore, as it is explained later, EOT nullifies the classical aperture theory proposed by Bethe. This unexpectedly high transmission enhancement can have numerous applications in photolithography, near-field microscopy, and nano-photonic devices.

The main contribution to the EOT in slits originates from two theories. First, the enhanced transmission results in the surface plasmons (SPs) that are generated from the oscillation of surface charges at metal and air interface. These SPs are generated if the momentum of the incident photons matches with the momentum of the oscillating charges of the slit [110, 111]. The second theory implies that a Fabry-Perot resonator is formed inside the slit (Figure 2.14(a)). Two up and down openings of slit act as a Fabry–Perot cavity which can enhance or suppress the transmission of the passing light through the slit (Figure 2.14(b)) [97].

Two important clues relating this phenomenon to SPs come from the following observations. Ebbesen et al. [110] reported the absence of enhanced transmission in fabricated hole arrays in Ge films, which points to the importance of utilizing metal in the structure of the slit. The other clue is the dependence of transmitted light intensity to the angle of the incident light to the metallic slit. This is exactly the same behaviour observed when light couples with SPs in gratings [112]. This proves the role of SPs in the observed enhanced transmission through the designed aperture [110]. Figure 2.16 shows an example of EOT, where authors were able to report an enhancement up to 10 times by optimizing the slit material and dimensions.

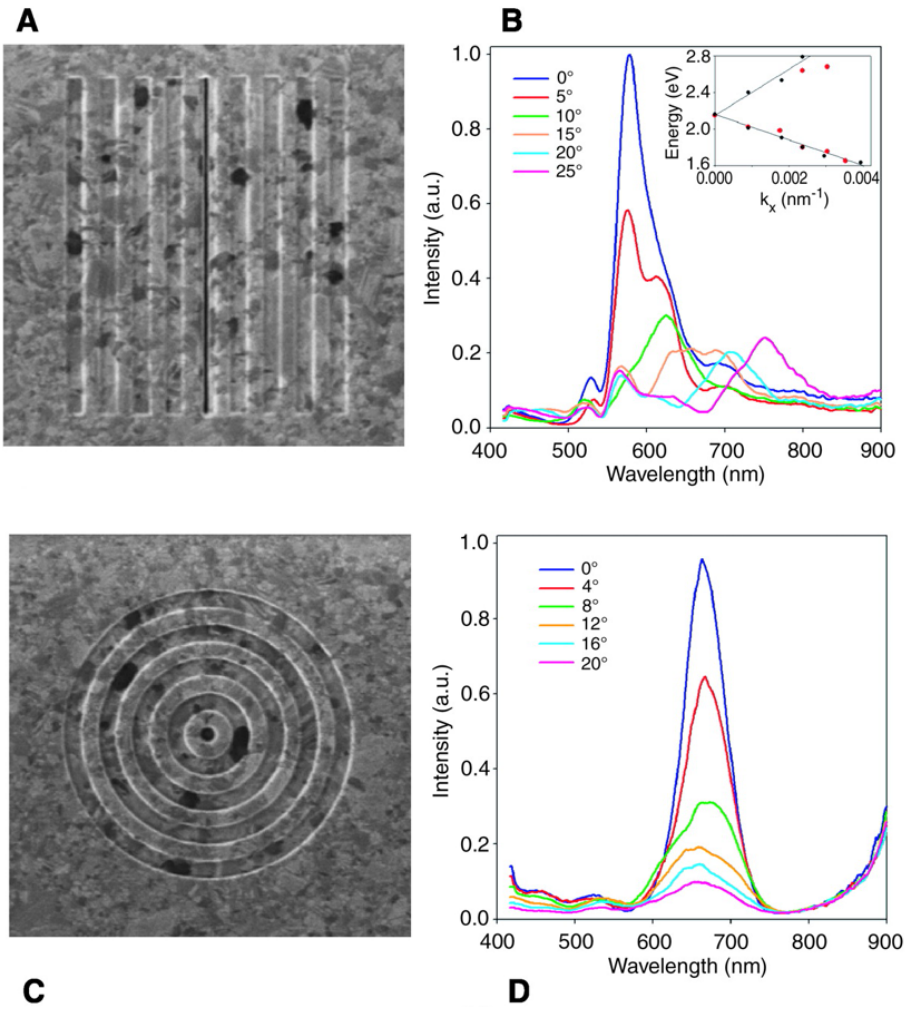

Figure 2.16. *An EOT with an enhancement of up to 10 times is measured.* ***a)*** *An image is taken from a slit aperture milled in 300 nm silver coating. The slit width is 40 nm with 4400 nm, length and both sides of slit have grooves with a depth of 60 nm and 400 nm period.* ***b)*** *Transmission spectra of the structure of slit from different collection angles. Illumination at normal incidence with perpendicularly polarized light to the slit-length direction (TM).* ***c)*** *An image is taken from a bull's eye aperture milled in 300 nm silver coating (groove periodicity of 600 nm; groove depth of 60 nm; hole diameter of 300 nm, 250 nm; film thickness of 300 nm).* ***d)*** *Transmission spectra of the bull's eye structure from different collection angles. The structure is irradiated at perpendicular incidence with unpolarized collimated light [109].*

For periodic perturbations in the form of sub-wavelength openings in a metal film, surface plasmon polaritons (SPPs) propagate along the incidence surface and couple to the transmitting surface through these openings. Surface plasmons are then converted back to photons on the transmitting surface and reradiated in the same direction as the incident beam [113].

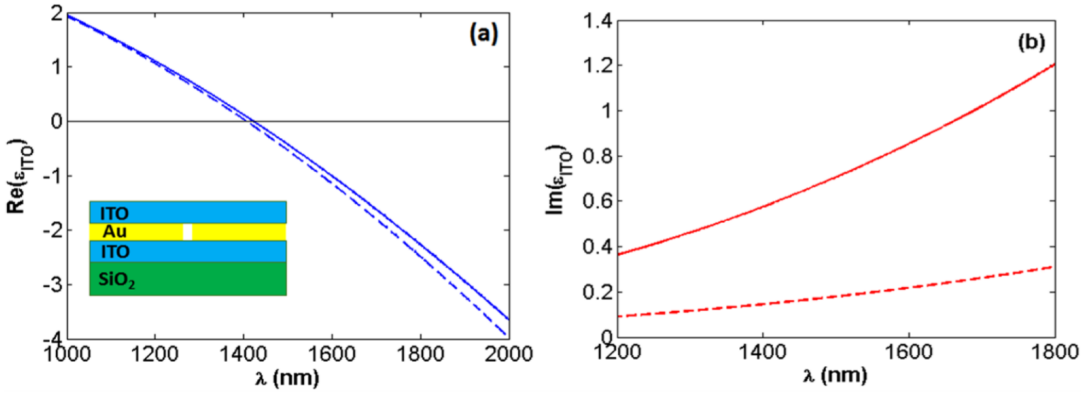

Figure 2.17. a) *Simulation of the real part of the permittivity for the used ITO in the structure of an ENZ based aperture. The solid blue curve is a realistic ITO, while the dashed blue curve is for the low-loss ITO. The figure inset shows the designed slit, which is placed between two ITO thin films.* ***b)*** *Calculated transmission for the designed aperture in different cases: the bare aperture (black-dotted), ENZ/Aperture system (dashed-red), ENZ/Aperture/ENZ hybrid structure (solid-blue) [114].*

Furthermore, it is possible to enhance the transmission of light with an ENZ metamaterial without using SPPs. Figure 2.17 (a), shows a subwavelength Au slit with a width of 300 nm and thickness of 50 nm, which is sandwiched between two thin layers of ITO (80 nm). Also, the real part of the permittivity of ITO is presented in this Figure, which shows an ENZ wavelength around 1415 nm. As It is shown in Figure 2.17 (b), adding an ENZ layer to the inner and outer sides of the single slit leads to achieve an enhanced and directional transmitted light through the designed slit [114].

3 METHODS

In this chapter, the numerical methods and simulations used in describing the subwavelength slit and later subwavelength slit over an ENZ substrate are explained. The fabrication and characterization processes are expressed briefly.

3.1 Simulation

FDTD method

The finite-difference time-domain (FDTD) method is used to solve the time-dependent Maxwell's equations in a spatially finite computation domain, which was introduced in 1966 by Kane S. Yee. This method solves Maxwell's equations in the differential form using a central difference operator in time and space simultaneously. The representation of electric and magnetic fields is applied to the spatial grid, and then the time evolution is performed. The four Maxwell's equations used to describe the behavior of electromagnetic fields are written as [115]:

$$\begin{aligned} \nabla \cdot \mathbf{D}(\mathbf{r},t) &= \rho(\mathbf{r},t) \\ \nabla \cdot \mathbf{B}(\mathbf{r},t) &= 0 \\ \nabla \times \mathbf{E}(\mathbf{r},t) &= -\frac{\partial}{\partial t}\mathbf{B}(\mathbf{r},t) \\ \nabla \times \mathbf{H}(\mathbf{r},t) &= \frac{\partial}{\partial t}\mathbf{D}(\mathbf{r},t) + \mathbf{J}(\mathbf{r},t) \end{aligned} \tag{3.1}$$

where $\mathbf{D}$ is the electric flux density, $\mathbf{E}$ is the electric field, $\mathbf{B}$ is the magnetic flux density, $\mathbf{H}$ is the magnetic field, ρ is the electric charge density, $\mathbf{J}$ is the electric current density, $\mathbf{r}$ is the position vector and t shows the time. By taking the divergence of fourth Maxwell's and using the first equation, one can obtain the relationship between the charge and the current density:

$$\nabla \cdot \mathbf{J}(\mathbf{r},t) + \frac{\partial}{\partial t}\rho(\mathbf{r},t) = 0 \tag{3.2}$$

The above equation is known as the conservation law for the electric charge and current densities. As it was explained in Chapter 2, when a medium is placed inside an electromagnetic field, three phenomena of conduction, polarization, and magnetization may

occur. According to these phenomena, the constitutive relations are written as

$$\mathbf{D}(\mathbf{r},t) = \varepsilon_0\mathbf{E}(\mathbf{r},t) + \mathbf{P}(\mathbf{r},t)\mathbf{B}(\mathbf{r},t) = \mu_0\mathbf{H}(\mathbf{r},t) + \mu_0\mathbf{M}(\mathbf{r},t) \tag{3.3}$$

where $\mathbf{M}$ is the magnetization density. For a nondispersive medium, the above equation 3.3, can be written as $\mathbf{P} = \epsilon_0(\epsilon_r - 1)\mathbf{E}$ where ϵ_r is the relative permittivity.

The boundary conditions show the variation of a field quantity which crosses the interface between two media. One can write the boundary conditions from Maxwell's equations as:

$$\begin{aligned}
\hat{\mathbf{n}}_1 \times (\mathbf{E}_1 - \mathbf{E}_2) &= \mathbf{0} \\
\hat{\mathbf{n}}_1 \times (\mathbf{H}_1 - \mathbf{H}_2) &= \mathbf{K} \\
\hat{\mathbf{n}}_1 \cdot (\mathbf{D}_1 - \mathbf{D}_2) &= \rho_s \\
\hat{\mathbf{n}}_1 \cdot (\mathbf{B}_1 - \mathbf{B}_2) &= 0
\end{aligned} \tag{3.4}$$

where $\hat{\mathbf{n_1}}$ is the unit vector perpendicular to the interface between the two media, pointing from the interface towards the first media and ρ is the surface charge density. $\mathbf{K}$ shows the surface current density, which is non-zero only on the surface of a perfect electric conductor (PEC). The filled quantities with subscript 1 are quantities inside the first medium close to the interface, and the field quantities with the subscript 2 are the opposite fields in the second medium.

The $\mathbf{D}$ Vector is continues across the boundary, and this continuity is due to the surface charges that produce a local field in the region. The continuity of the $\mathbf{D}$ field denotes that the normal component of the $\mathbf{E}$ should be discontinued across the interface.

Yee's algorithm

The position and orientation of $\mathbf{E}$ and $\mathbf{H}$ fields inside the spatial unit cell in a three-dimensional FDTD are illustrated in Figure 3.1. If several neighboring cells form an FDTD lattice, then for each one of the $\mathbf{E}$-field components, there will be four circulating components of the $\mathbf{H}$-field. The reverse is also true for each one of the $\mathbf{H}$-field components. This kind of division of space as lattice originates from Maxwell's equations, which are written in the curl form for Faraday's and Ampere's laws [115]. When the first and second Maxwell's equations are written in a partial form, one can obtain six scalar equations [116].

A mesh is defined by grid points of $(i,j,k) \equiv (i\Delta x, j\Delta y, k\Delta z)$. In the meantime, a scalar function of space and time is defined as $F|^n_{i,j,k} \equiv F(i\Delta x, j\Delta y, k\Delta z, n\Delta t)$. Where Δx,Δy,Δz, are spacial increments and Δt is the time increment, and i j k n are integers. Yee used second-order accurate central finite differences to discretize the partial space and time derivative equations. In the next step, time-domain evolution is used on the $\mathbf{E}$ and $\mathbf{H}$ fields. Yee's formulas are written in the time domain and can be used for time-harmonic electromagnetic fields or propagated pulsed fields [116].

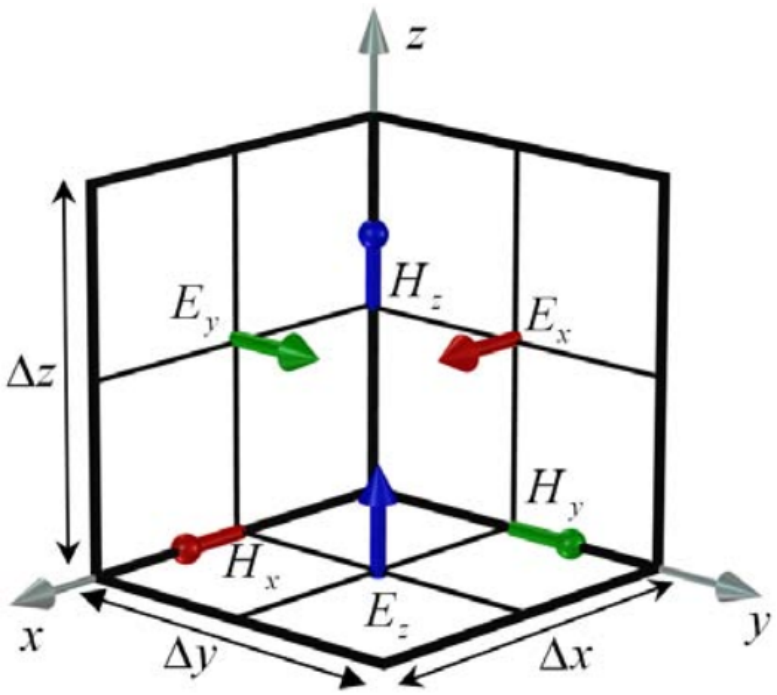

Figure 3.1. *Locations of the electric and magnetic field components in a unit Yee cell with dimensions* $\Delta x, \Delta y, \Delta z$ *[115].*

Lumerical FDTD Solutions

Simulations are conducted utilizing an FDTD method, implemented with the aid of a commercial software package (Lumerical FDTD Solutions). Gold nanostructures with various diameters are modeled with a frequency-dependent dielectric function taken from Johnson and Christy [117], while 40 nm ITO is simulated using the reported data in Ref. [118].

For field simulations, the incident field is a transverse electromagnetic total-field scattered-field (TFSF), propagating in the Y direction, with electric and magnetic fields in X and Y directions, respectively. The normalized field profiles were calculated at the maximum transmission wavelength and plotted in the XY cross-section plane. In transmittance simulations, the transmitted signal is collected at 1.5 um far from the slit's surface. A field monitor is placed with a "2D-Z normal" orientation to measure the electric field and Poynting vectors. For a faster simulation, the antisymmetric boundary condition was used in the x-axis, centered in zero. Figures 3.2 and 3.3 are FDTD simulation's setup and design for fabrication of samples, respectively.

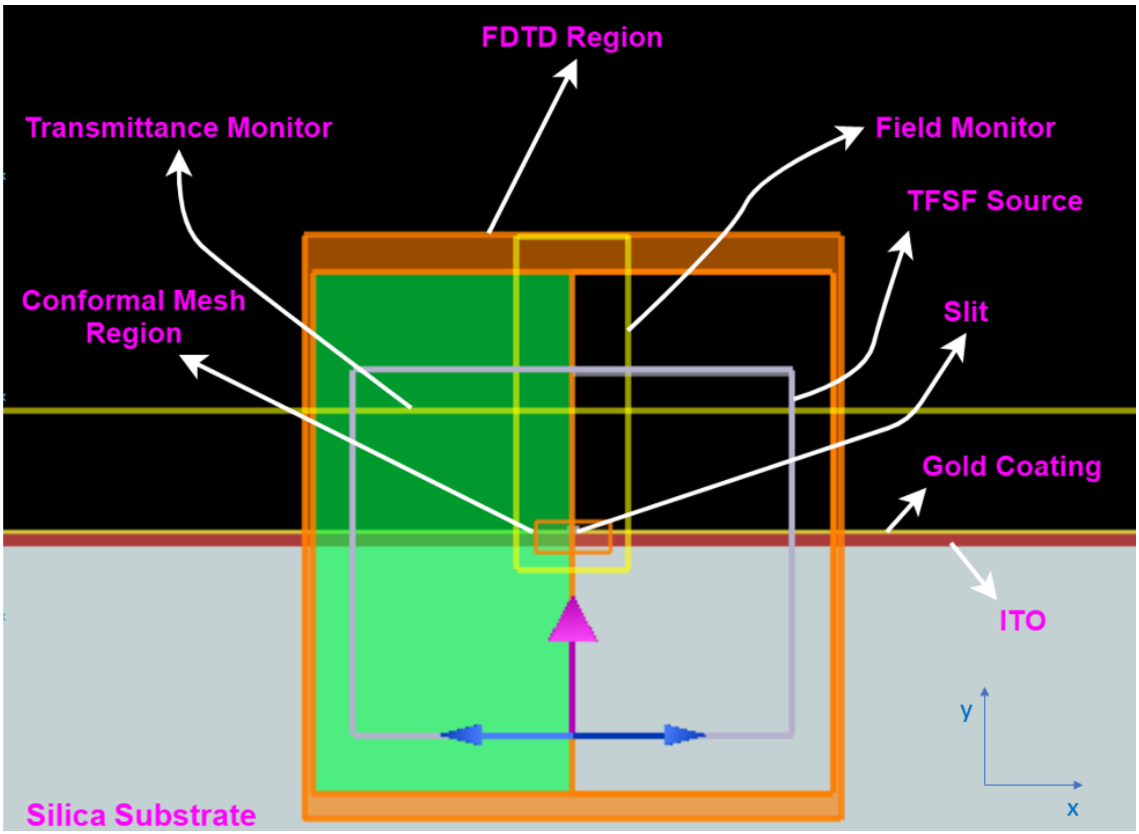

Figure 3.2. *FDTD simulation setup and respective elements.*

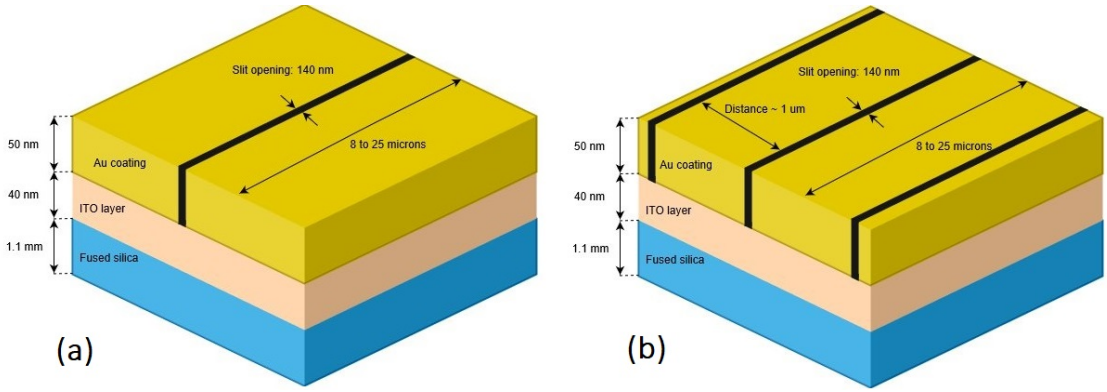

Figure 3.3. ***a)*** *Design for a single slit opening in a gold substrate over ITO layer.* ***b)*** *Design for three slits opening in a gold substrate over ITO layer. Both structures use silica as substrate.*

3.2 Fabrication

A fused silica (SiO_2) with a thickness of 1.1 mm is used as a substrate to fabricate samples due to the small refractive index and high transparency. The first step before starting the main fabrication process is cleaning the substrates. It is imperative to clean the samples thoroughly to eliminate any unwanted contamination samples. These impurities come in the form of organic and inorganic particles (or thin-film in case of a protective layer over the substrate). Substrates are first cleaned with soaking them in acetone,

which is very potent in removing organic and nonorganic impurities. Then samples are soaked inside isopropanol(Isopropyl alcohol) and later dried with nitrogen blow. Afterward, the substrates are sonicated for 20 minutes inside an acetone bath, then the first cleaning process is repeated before using the oxygen reactive ion etching (RIE) machine as the last step of the cleaning process. The reason for cleaning with acetone before IPA is the faster evaporation of the acetone, which prevents leaving any evaporated solvent stains on the substrates. As the last step, the RIE method is used for 10 minutes to remove any probable remaining microscopic contamination. After visually inspecting samples with an optical microscope, they are used in the fabrication process. The samples with 40 nm of ITO are purchased from Präzisions Glas & Optik GmbH (Iserlohn, Germany). The metalization process is completed by depositing a 50 nm thick gold layer using an E-beam evaporator machine at a rate of 0.02 nm/sec and a vacuum pressure of 5.6 $\times 10^{-6}$ mbar.

E-beam evaporator

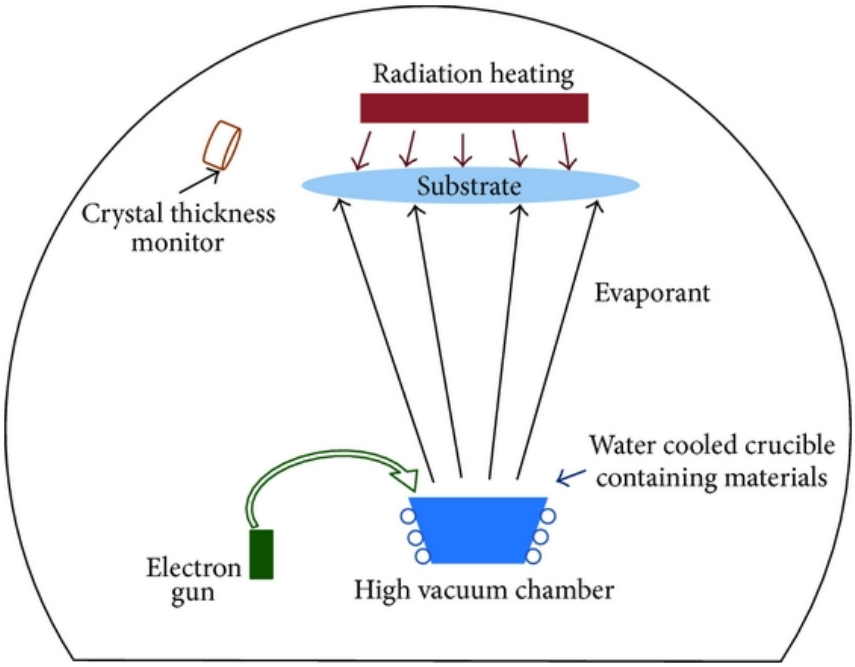

Figure 3.4. *Illustration of an e-beam evaporator source [119].*

E-beam evaporator machine, as a physical vapor deposition method, is used for a thin and accurate metalization process. Figure 3.4 illustrates a scheme for an e-beam evaporator. The design of the metal evaporator machine allows us to separate the sample chamber from the crucibles chamber. Therefore, the influence of the electron beam heat on the physical properties of the samples is minimized. Both chambers of this device are kept under vacuum conditions during the metalization process. During the entire deposition process, the sample chamber is cooled down below room temperature with the continuous flow of cold water. The cooling of the sample is done to increase the cohesion

of particles to the substrate during the precipitation process.

The device consists of several crucibles containing different metallic materials. The high voltage and current controlled tungsten filament emit electrons, which in return bombards the crucible and evaporates the metal inside it. The evaporated material particles move with high speed toward all directions inside the chamber and coat all sides, including the sample [120].

A quartz crystal is used as a thickness monitor. The crystal's mass is changed by deposition and changes the vibrations. This helps one to track the deposition accurately over each second. Because the thickness is known in every moment, the rate of deposition is calculated automatically, and it is possible to change the rate of deposition by changing the feed current of the beam source. In our work, we first used low rates as low as 0.01 nm/sec, and after forming a 5 nm gold layer, it was increased to 0.2 nm/sec. The whole process was done under 9 $\times 10^{-6}$ mbar vacuum pressure, and operating voltage is kept as 7.28 kV.

Focused Ion Beam

Focused Ion Beam (FIB) lithography uses charged particles to remove material and etch the surface in nanometer scales. The process is visible in real-time during the etching. The bold disadvantage of FIB is irreversibility. Not only the etching is irreversible, but the imaging with FIB changes the surface with the same effect. Usually, an FIB system has dual beams: an electron beam for imaging and positioning the sample and an ion beam for patterning (Figure 3.5 (a)). Gallium is the source of choice in many cases due to the easy extraction of ions from the low melting point (300° C) liquid metal. In an operational FIB device, Ga^+ ions are melted and accelerated towards the target for either imaging or etching. This charge must be grounded with a conductive layer on the target sample. The conductive layer is often grounded using colloidal graphite applied on the edge of the sample [121]. Materials that have low conductivity can bring complications to the process. Simultaneously, there is gallium contamination during the etching of the target, and with a minimized similar effect for imaging.

A Zeiss Crossbeam 540 FIB is used to mill the samples. The acceleration energy of Gallium ions is 30 keV. The ion current used in the experiments is not determined because the current was not calibrated, but 1 pA probe was used. This is the lowest possible current that can be generated by the system and has the least damage to the sample during imaging and aligning.
The etching time depends on the thickness of the layer, but it is usually in the orders of a few minutes. For metals, focused ion beamed surfaces often become rough, because differently oriented grains have different etching yields. Figure 3.5 (b) shows this ion-beam induced roughness for a 50 nm thick gold film.

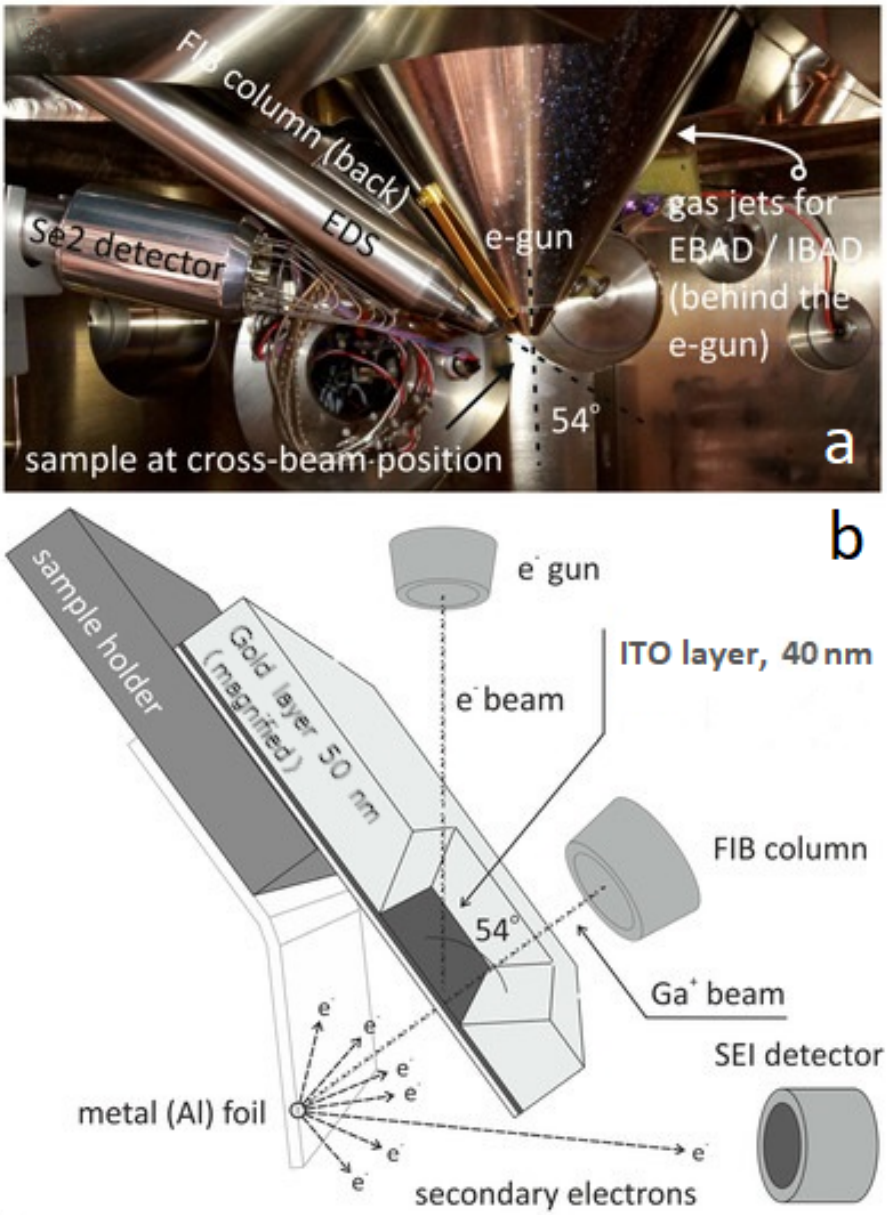

Figure 3.5. ***a)*** *Picture for different components of an FIB machine used for milling the gold layer.* ***b)*** *Schematic of an FIB setup [122].*

3.3 Characterization

Transmittance measurements are performed on a multi-functional WITec alpha300C confocal Raman microscopy system. A scheme and image of the setup to characterize the fabricated samples are presented in Figure 3.6 (a) and (b), respectively. For transmittance measurements, the samples are illuminated using a highly bright and stable broadband light source (LDLS EQ-99X) provided by Energetiq through a Zeiss "Epiplan -Neofluar" 50 X Objective (NA=0.55 WD=9.1mm). The transmitted light is collected through a Zeiss EC ”Epiplan” DIC, 50 X air objective (NA=0.75, WD=1.0 mm) and is launched to a fiber-coupled NIR detector provided by Ocean Insight. The transmittance spectra (Tra) are

calculated according to the following formula :

$$Tra = \frac{I_{trans} - I_{BG}}{I_{sub} - I_{BG}} \tag{3.5}$$

where I_{BG} stands for the background counts, acquired by the used system, I_{trans} is the intensity of the transmitted beam through control (slit) and main (slit on ITO layer) samples, and I_{sub} is referred to the intensity of the transmitted beam through the substrate. One need to take into account that for the control sample, the substrate is considered as glass, while for the main sample, it is considered as ITO on the glass.

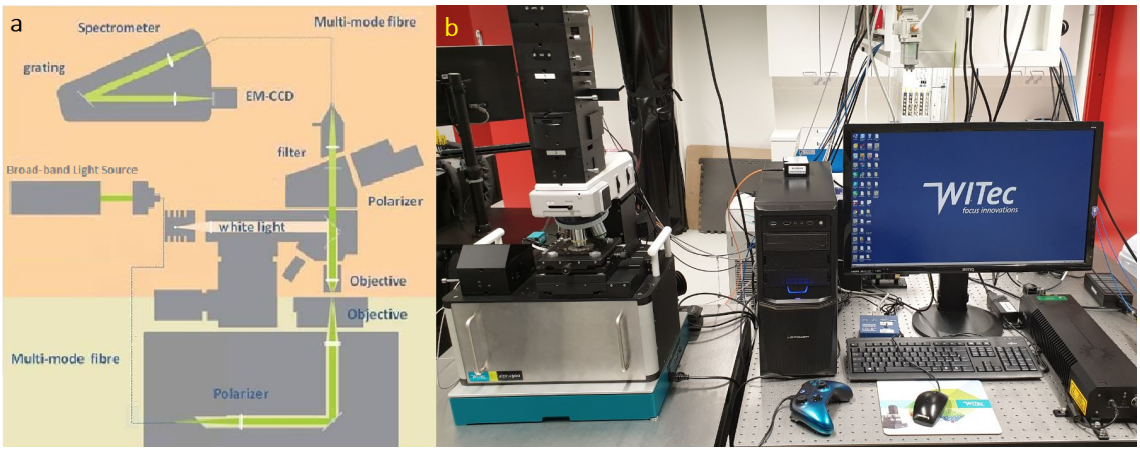

Figure 3.6. ***a)*** *Schematic of WiTec microscope used in the characterization of the fabricated samples.* ***b)*** *Picture of the applied setup.*

4 RESULTS AND DISCUSSION

4.1 Optical features of ITO film

The transmittance and reflectance for a 40 nm thick ITO film are measured using the WiTec confocal microscope and are presented in Figure 4.1. The high transmittance and low reflectance values are evidence for a low absorbance of the ENZ material in the desired spectral range. This guaranties the lower values for the extinction of the ITO as the absorptive part of the refractive index, which creates the opportunity for the pro missing practical applications.

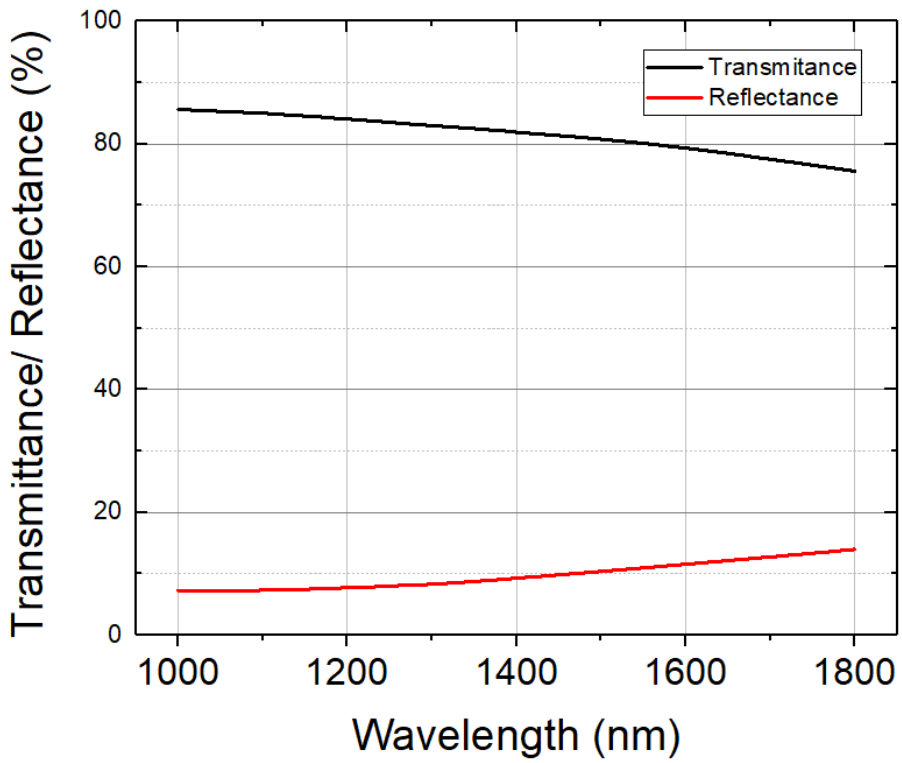

Figure 4.1. *Transmittance and reflectance spectra of 40 nm ITO film. The measured parameters are used to obtain optical properties of the ITO thin film using a fit procedure.*

To determine permittivity, ITO is defined as a plasma material based on the Drude model in Lumerical software. The initial definition for ITO had a ϵ_∞=3.91 permittivity with a plasma resonance (ω_p) of 2.65×10^{15} rad/s and a plasma collision frequency (ω_d) of 2.05×10^{14} rad/s. Later the transmittance is simulated by placing frequency monitors that record

the output power in the y-direction on both sides of the sample, while the reflectance is calculated by considering the light source and frequency monitor on top of the ITO film. The mentioned Drude parameters to determine ITO's permittivity in Lumerical software are adjusted in such a way that the simulated results fit with the acquired experimental transmittance and reflectance. Final fits for refractive index and permittivity are presented in Figure 4.2. It is discussed before in section 2.3 that for a lossy material, the ENZ wavelength is determined in the point that both the real and imaginary values of the dielectric constant get equal. As is noticeable in Figure 4.2 (a), n and k parameters of the ITO film have the same value of 0.57 at the wavelength of 1400 nm. This ENZ wavelength is evident in the plot of the primitively, presented in Figure 4.2 (b).

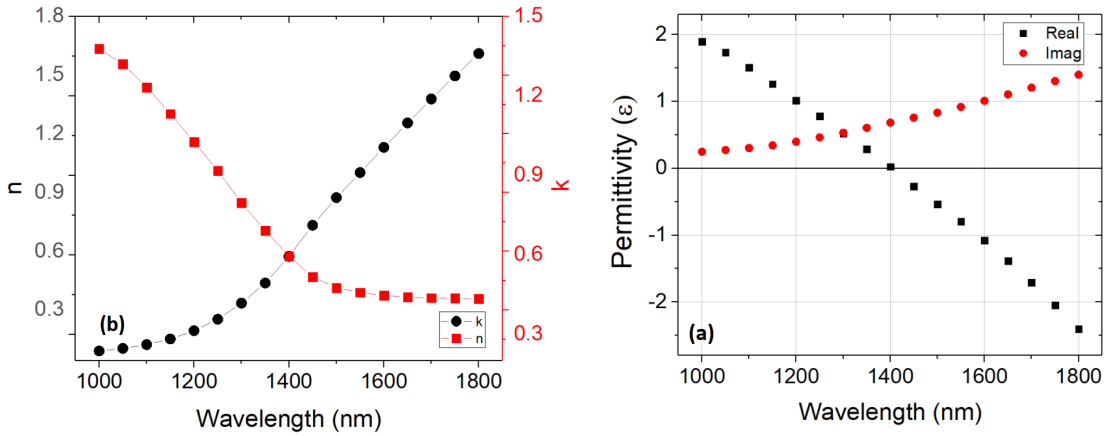

Figure 4.2. a) *Refractive index and extinction coefficient extracted for the ITO film using a fit procedure for FDTD simulation.* ***b)*** *Corresponding real and imaginary parts of the permittivity.*

4.2 Single slit

For the first step in simulations, the mentioned layout in Figure 3.2 is established in a 2D configuration. In all simulations, a substrate of Silica with 40 nm of ITO coating is referred to as the "ITO layer". All the apertures are designed in a 50 nm thick gold layer deposited on top of a glass substrate or ITO thin film. The thin design of the top coating is due to the main reason for facilitating the fabrication process with the FIB machine. Thicker layers of metal increase the chance of damage to the thin ITO layer during the milling process. Moreover, the thick metal layer can cause the fabrication process to end up in a slit with curved walls, instead of designed sharp walls.

As the wavelength of the study was set from 950 nm to 1650 nm, the extreme subwavelength region dictated constraints on slit width. Accordingly, the slit width is selected as a value between 100 nm to 170 nm. Afterward, the transmittance through the designed slit is recorded by monitors. The transmittance of a plane wave (TFSF) through a single slit in the spectral study range is presented in Figure 4.3. As one can see in panel (a), the transmittance for slit width less than 130 nm is dropped significantly. Later, a 40 nm ITO layer is added under the slit and the calculated transmittance is presented in Fig-

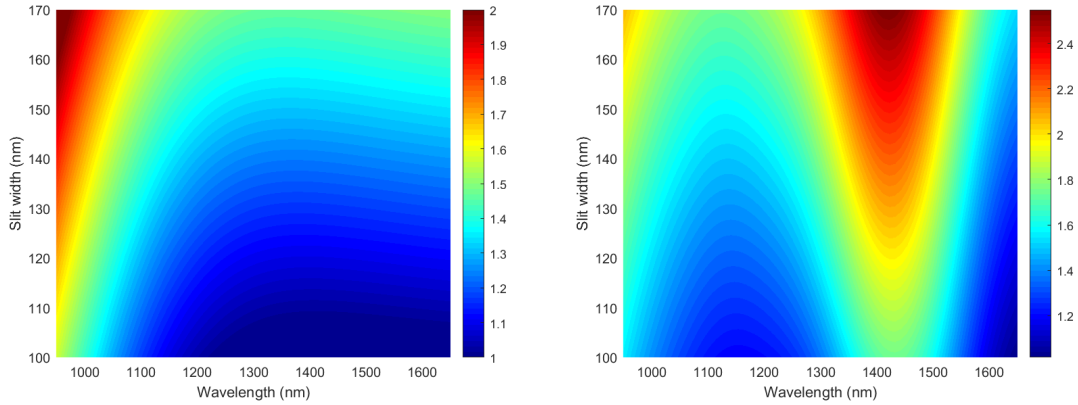

Figure 4.3. a) *Transmittance achieved in FDTD simulations for a single slit with varying width and in the absence of ITO,* ***b)*** *in the presence of a 40 nm ITO layer.*

ure 4.3 (b). One can see that light transmission near the ENZ region (1300-1500 nm) is enhanced.

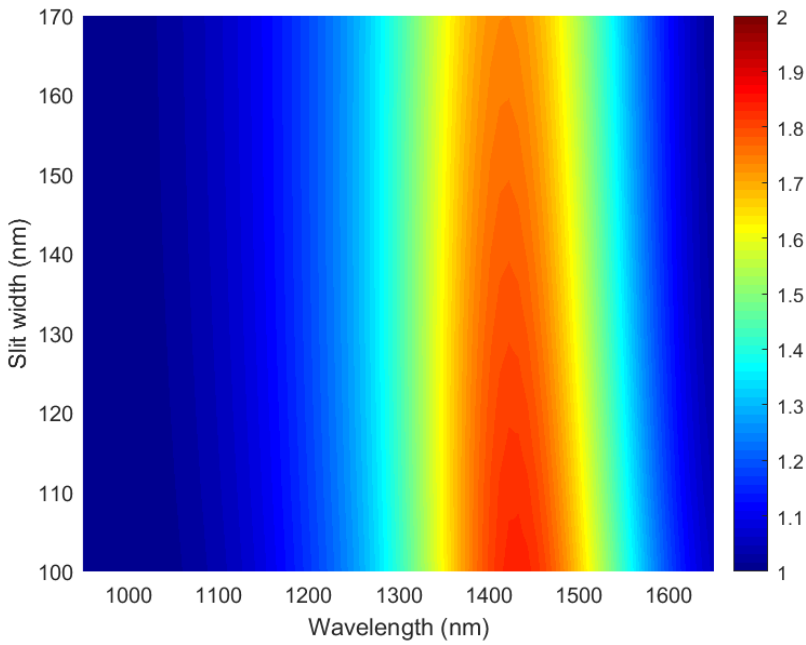

Figure 4.4. *The calculated enhancement factor for an ENZ based single slit structure. The ENZ region (1300 nm -1500 nm) shows higher transmittance after adding the ITO layer. The enhancement factor is calculated by dividing the transmittance of a single slit with the ITO layer to the transmittance of the corresponding structure without an ITO layer.*

The ratio of the transmission intensity for the slit in the presence and the absence of the ITO layer is shown in Figure 4.4. The calculated ratio refers to the enhancement factor of the transmittance, while the ENZ material is added to the beneath of the designed slit. One can spot the fact that the enhancement is maximum in the ENZ region for slit width less than 130 nm. However, due to low transmittance and difficulty in experimental measurement, a slit width of 140 nm is chosen to study light enhancement in all designs of this thesis. For such a width value of a single slit, the transmittance enhancement factor

is 1.8 (Figure 4.4). The maximum transmittance happens at 1400 nm, which corresponds to ENZ point.

Poynting vector analysis

Field profiles for Poynting vector, intensity, and **E** are calculated in Lumerical using the FDTD method to understand the underlying reasons for the observed enhancement.

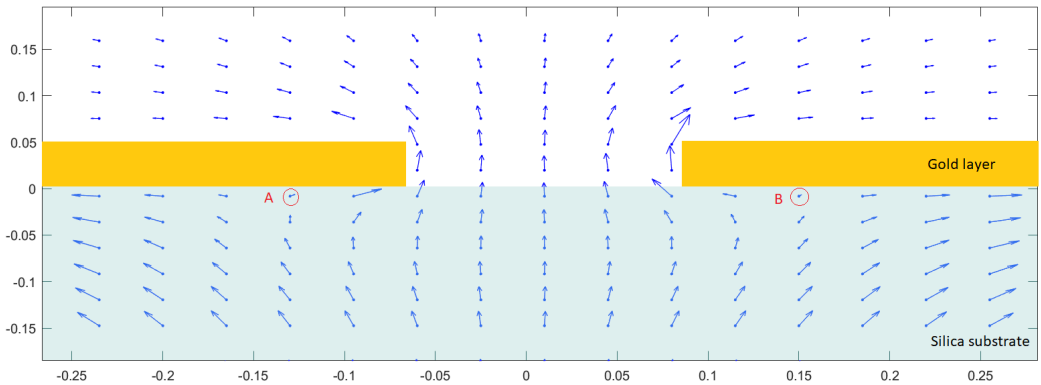

Figure 4.5. *Orientation and length of Poynting vectors. In marked points A and B, the length of the Poynting vector is zero and power flow is moving in two opposite directions forming a half saddle. The calculation is performed at the* λ_{ENZ} *= 1400 nm for a slit width of 140 nm.*

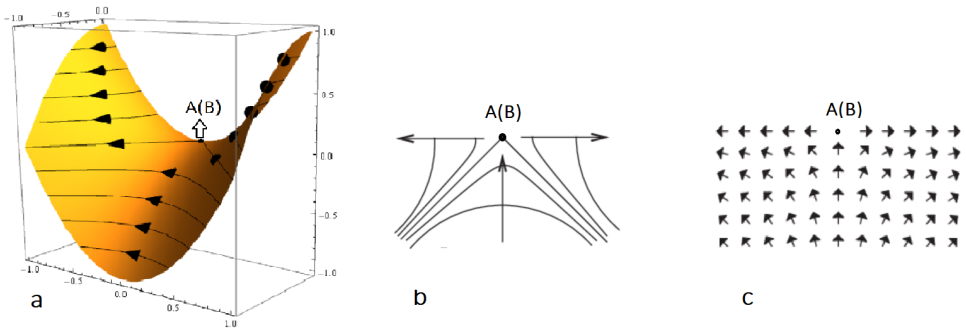

Figure 4.6. *Phase and power flow formation near the slit in points A and B shows singular points of the phase.* ***a)*** *3D visualizing contour for points with the same phase,* ***b)*** *2D top view of the contour,* ***c)*** *power flow.*

Figure 4.5 presents Poynting vectors for a single slit etched in a gold layer over a silica substrate. It is seen that in points A and B marked with red circles, there are spots of Poynting vector with zero length. These points represent areas with zero intensity or magnitude for the Poynting vector. The power flow forms a half saddle in these two marked areas with a singularity in the phase of the propagating electromagnetic field. These points are illustrated in Figure 4.6. At these points, the phase is infinitely undetermined and it is shown that phase singularities hinder the transmittance of light through subwavelength slits [123]. Those singularities prevent the smooth flow of energy near the slit and annihilation of them will increase the total transmittance of the slit [92].

Figure 4.7 represents the occasion when an ITO layer is introduced to the single slit

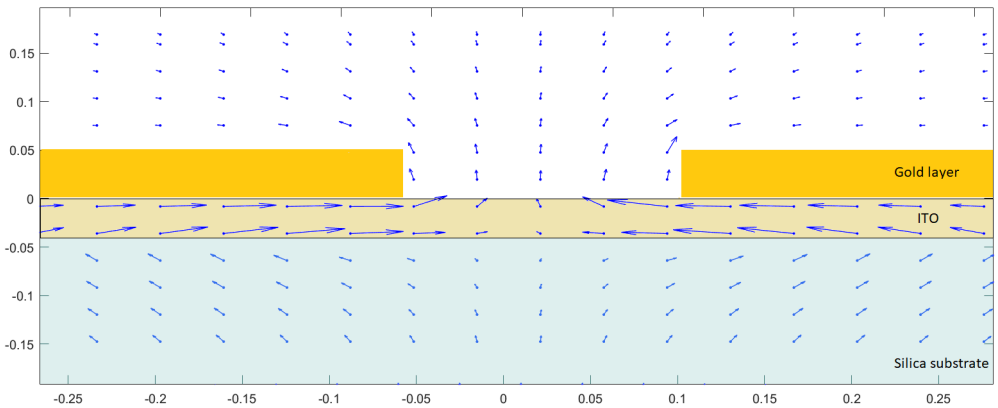

Figure 4.7. *Orientation and length of Poynting vectors. Due to the presence of the ENZ layer, the singularities in points A and B are eliminated. Note that the energy flow in the glass does not decrease noticeably and vectors become shorter due to the normalization regarding the substantial increase of energy flow in the ENZ layer. The calculation is performed at the* λ_{ENZ} *= 1400 nm for a slit width of 140 nm.*

structure. One can see that the ITO layer enhances the electric field and at the same time, eliminates two observed phase singularities in the case of the single slit on the glass substrate. The presence of the ENZ metamaterial eliminates the optical vortices (zero of the optical fields; phase singularity) and leads to a smoother electromagnetic field with higher transmittance through the slit.

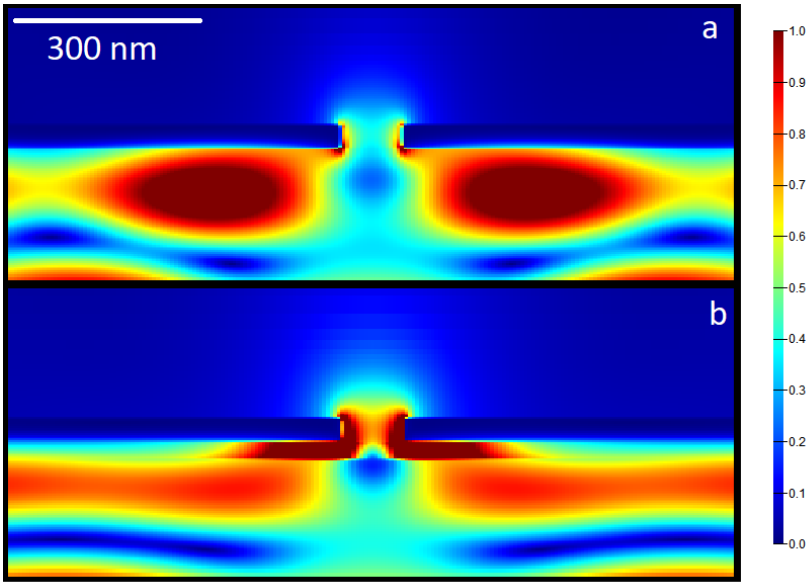

Figure 4.8. *The magnitude of the Poynting vector is reproduced using FDTD method.* ***a)*** *Single 140 nm slit in gold layer (50 nm).* ***b)*** *A layer of ITO (40 nm) is added to the previous structure. As one can see the main increase in the intensity is for rims of the slits, with the highest contribution for increasing the intensity and resulting in EOT. This figure is plotted at* λ_{ENZ} *= 1400 nm.*

Figure 4.8 is a depiction of the magnitude of the Poynting vectors, which helps to see the light funneling and transmission in the slit. The presence of the ITO layer under the metallic slit significantly increases the out-coupling efficiency of the electric field by the aperture to the far-field [3]. This occurs due to the significant amplification of the electromagnetic fields inside the ENZ medium [31, 124].

Electric field analysis

The profile of the electric fields in the x- and y-directions are analyzed in this section. Figure 4.9 (a) and (b) shows the electric field in the x-direction. In these two panels, the spectrum of red color to yellow indicates a vector towards the right side of the x axis (+x), while the spectrum from blue to cyan signifies the opposite direction (-x). One can see there is an electric field with a direction from left wall to the right wall of the slit. This indicates the presence of the LSP mode (cavity mode) in the air gap of the designed slit. One need to note that only for TM polarization of the incident light, the surface charges can be induced on the walls of the slit. These induced charges are in opposite phases at two sides of the slit [125, 126]. Consequently, an electric field spanning from a positive to a negative charge is formed, resulting in an efficient out-coupling of the light through the slit [115, 127].

Another way of explaining this phenomenon is by using the slit waveguide modes via the standard waveguide theories [115]. The TM_0 mode propagating in the slit is guided through the slit via surface charges and currents, which experience the slit lower (entrance) and upper (exit) interfaces and produce a TM_0 field which reflects back towards the lower side of the slit. The propagated TM_0 wave interacts with its reflected component in which depending on the waveguide length, different intensities of the superpositioned TM_0 waves can be produced. It is worth to notify that here the waveguide length corresponds to the thickness of the gold film. The reflectivity of the lower and upper sides of the slit is due to the significant difference between the effective index of the waveguide mode propagating through the slit and the refractive index of the surrounding medium [128, 129]. The waveguide modes and occurring variations due to different Au layer thickness are not studied in this work because of the extra complexity that can be introduced to explain the observed enhancement.

Figure 4.9 (b) shows a stronger LSP mode between the walls of the slit, as it is placed on top of the ENZ material. As is evident in Figure 4.8 (b) the magnitude of the Poynting vectors is enhanced, when the ITO is introduced under the slit. The annihilation of the phase singularities in the presence of the ITO enhances the transmission and intensifies the electromagnetic field through the slit. Consequently, the presence of the ENZ material leads to the formation of a stronger LSP modes in the air gaps of the metallic slit.

The electric field in the y-direction reveals the presence of SPPs. As one can see in Figure 4.9 (c) and (d), the electric field starts from positive surface charges and terminates in negative ones. Near the rims of the slit, SPPs are in the symmetric mode, which means

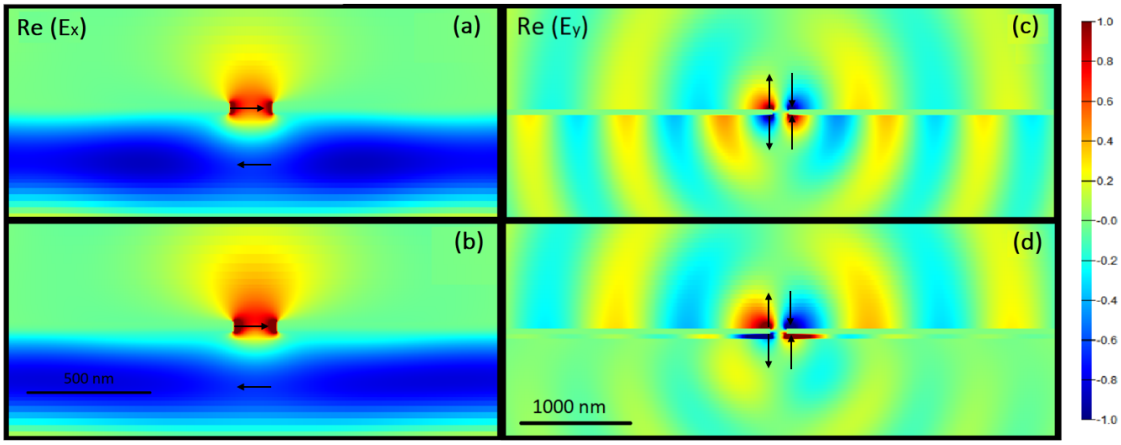

Figure 4.9. *Profile of the electric fields in the x-direction for a 140 nm slit opened in a gold film* ***a)*** *on a silica substrate,* ***b)*** *on a 40 nm ITO layer deposited over silica substrate. Red color indicates a vector towards the right (+x), while blue indicates the vector towards the left direction (-x). Profile of the electric fields in the y-direction for a 140 nm slit opened in a gold film* ***c)*** *on a silica substrate,* ***d)*** *on a 40 nm ITO layer over silica substrate. Red color indicates a vector towards the up (+y), while blue indicates the vector towards the down direction (-y). The arrows show the direction of the strongest respective electric fields (e.g., x,y) in the neighboring area. These calculations are performed at* λ_{ENZ} *= 1400 nm.*

that the surface charges are in the opposite phases at two sides of the film. Consequently, in this specific region, the electric field maintains its phase across the metallic film. It should be taken into account that due to the dielectric difference at the upper and lower interfaces of the Au film, the frequency of the generated PSPs is different. This leads to achieving an asymmetric mode, moving along the x-axis of the slit [2]. This means that the surface charges are in the same phase at two opposite sides of the gold film and thus the amplitude of the electric field component perpendicular to the film shows a zero inside the film. By changing the studied wavelength, one could see the PSPs are produced continuously in symmetric, asymmetric, and mixed modes. Note that in Figure 4.9 (c) and (d) due to low division of the conformal mesh, the fields farther than 1000 nm from the center of the slit could show alterations compared to real physical behavior. The comparison of SPP modes in panel (c) and (d) of Figure 4.9 show that the presence of the ENZ material enhances the PSPs in the interface of the metal and ITO. This occurs due to the strong field confinement inside the ITO, resulted from the imposed boundary conditions at the interface of the Au layer and the ENZ medium. ENZ medium supports only highly directive leaky waves, which means that the generated PSPs in the interface of metal-ITO can only penetrate into the glass substrate almost with a normal angle in the form of leaky modes.

Overall, the presence of the ENZ material leads to the annihilation of the phase singularity at the left and right of the lower side of the slit (Figure 4.5). Accordingly, this results in a formation of stronger PSP modes on inner surfaces of the slit and, therefore, a stronger LSP mode in the air gap of the slit due to the plasmon hybridization between these two modes [104, 130]. It should be taken into account that the formation and Subsequently

hybridization of the LSP and PSP modes occurs only for TM polarization, as the slit does not work as a subwavelength structure for TE polarization of the incident wave. Such strong localized and propagating surface plasmons act synergically, resulting in a strong funneling of the Poynting vectors near the walls of the slit as it can be vividly seen in Figure 4.8. The superposition of all discussed effects results in an EOT through the slit due to the presence of the ENZ metamaterial.

As it is mentioned in the background section (2.3.1, internal reflection) when an electromagnetic wave is incident to the ENZ material due to high refractive index and according to the Snell's law, this EM is going to be reflected back unless it is normal to the interface of these two surfaces. As it is explained, the slit acts as a waveguide and in the lower entrance of the slit the condition for internal reflection is satisfied. This implies that, the reflected beam from the end of the waveguide (top exit, at the same level with the surface of the film) has a great chance of total internal reflection. In conclusion, this contributes to the enhancement of the transmittance by the internal reflection of beam incident from air to ENZ material.

4.3 Several apertures

The study of triple slits (three slits) can help one to further understand the interaction between apertures. The main parameter in this part and three dimensional (3D) apertures is the distance between the openings. The slit width in all the linear and circular rings is fixed at 140 nm. This choice is made upon previous results for a single slit, as it was mentioned there is a trade-off between enhancement and transmittance for a slit. Accordingly, an appropriate opening for the slit would fit in 130 to 150 nm area. Simulations for three slits are done in a 2D FDTD Lumerical set up.

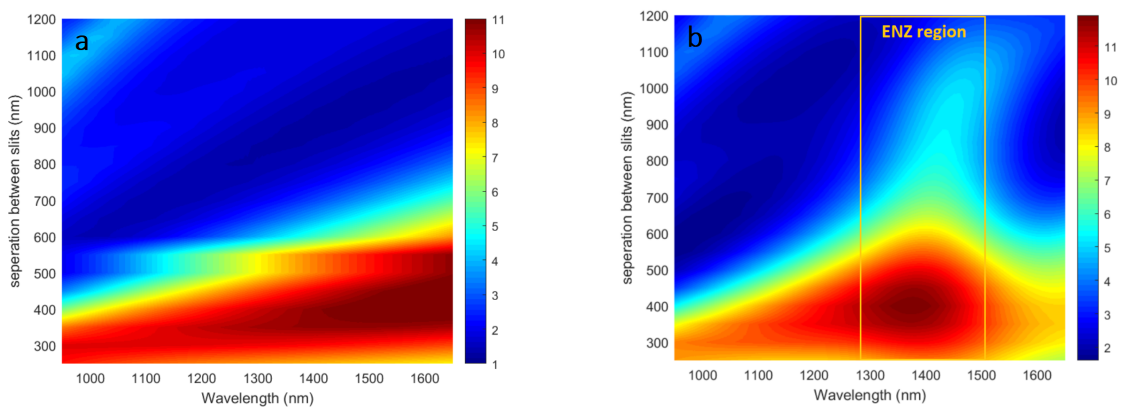

Figure 4.10. *Transmittance achieved in FDTD simulations for three slits with varying slit separation* ***a)*** *in the absence of ITO layer and* ***b)*** *in the presence of a 40 nm ITO film.*

A sweep function defined to change the distance between slits and to cover all this area, a conformal mesh region with the largest dimension is placed. The separation between the middle slit with two other side slits were varied in the range of 300 nm to 1200 nm with steps of 50 nm. The interest wavelength was kept in the spectral range of 950 nm to 1650

nm. Figure 4.10 (a) shows simulations results for transmittance of a TM polarized light through three slits in the absence of the ITO layer. One can see increasing the distance between slits leads to smaller transmittance. This is because of less interaction between slits; even for separation distances farther than 1000 nm, the interaction between slits becomes so weak that the total transmittance of slits gets similar to three single slits. Figure 4.10 (b) shows the transmittance of a TM polarized light through the same slits after adding a 40 nm of ITO layer. The footprint of ENZ material is easily visible in the 1300 to 1500 nm region. By dividing the transmittance values of the sample with ITO to the sample without ITO, one can acquire Figure 4.11 as the transmittance enhancement factor. The dark red area is a region with maximum enhancement.

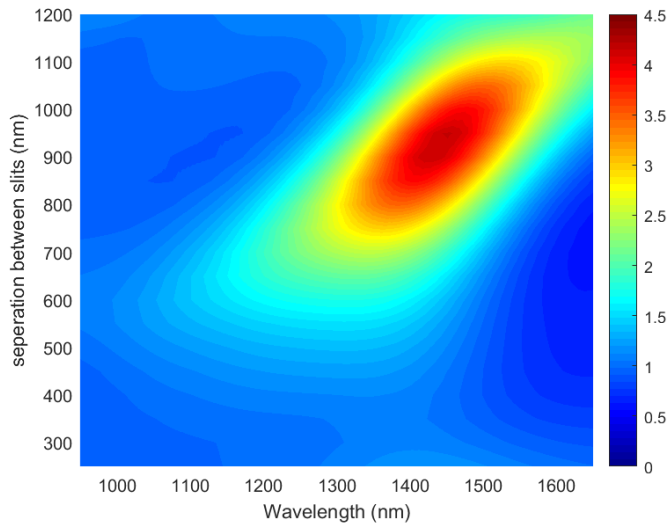

Figure 4.11. *Transmission enhancement factor of an ENZ based triple slits structure. In the ENZ region (1300 nm -1500 nm), higher transmittance enhancement is observable.*

In Figure 4.12 (a) E_y field for these three slits are presented for a case where they have placed 810 nm from each other (950 nm from centers). In Figure 4.12 (b) E_y field for these three slits with a same arrangement is simulated. The enhancement of fields inside the ITO and their symmetric PSPs formed in the upper surface of the Au film is clearly comprehensible. Comparison of Figure 4.12 with 4.9 shows the consistency of symmetric PSP formation in the fields. Unlike a single slit when the distance from slit is slightly increased, asymmetric PSPs are formed and they interact destructively with symmetric ones. For this particular reason, when several slits are placed next to each other it may be possible to achieve a higher or lower total transmittance as opposed to the sum of a single slit's transmittance. Theoretical studies suggest that enhancement (suppression) can result in a six (nine) times more (less) transmittance efficiency. If λ_{PSP} is defined as the wavelength of the surface plasmon polariton, one could expect dips of transmittance in multiple integers of λ_{PSP} (2λ_{PSP}, 3λ_{PSP},...). The peaks of efficient transmittance appear in between these values. It is ferreted out that increasing number of slits to more than four has an unsatisfactory effect on final transmittance [131].

The last simulation for three slits consists of time-averaged Poynting vector magnitude

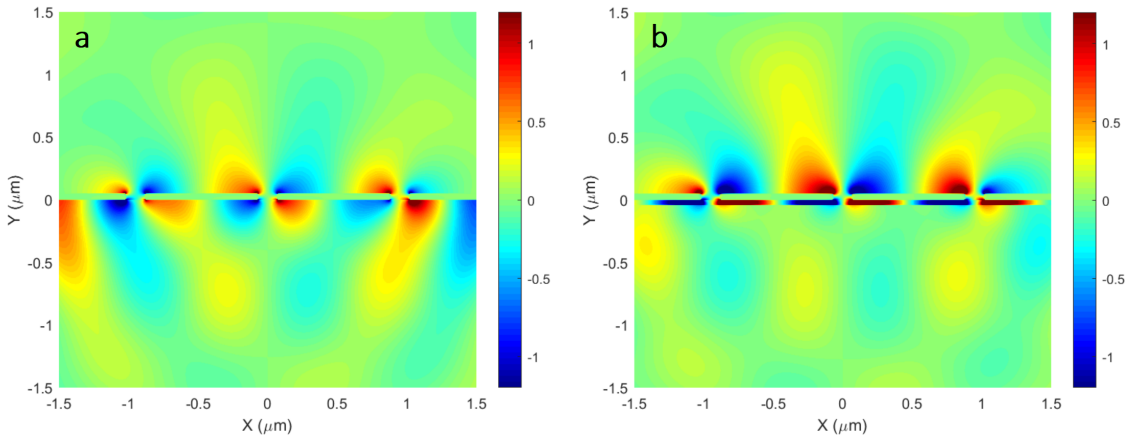

Figure 4.12. *Profiles of Ey of triple slits **a)** without ITO and **b)** in the presence of a 40 nm ITO layer.*

representation is exhibited in Figure 4.13. A similar formation of magnitude is seen. Even so, the more intense areas extend longer in the x-direction. The seen effects in several slits are similar to a single slit surrounded by parallel grooves. A good design of corrugations around the slit entrance enhances the light transmission under a perpendicular incident plane wave. An agreed explanation for this enhancement in a thin metal film is bonding (top and bottom) PSP modes that propagate on film's surfaces with a coupling to the aperture as a waveguide [132]. These modes can result in enhancement or suppression base on the phase difference between the modes [133]. Another enhancing factor is the generation of short-range fields that couple to the aperture. These fields are only possible within a few wavelength distances from the slit [134].

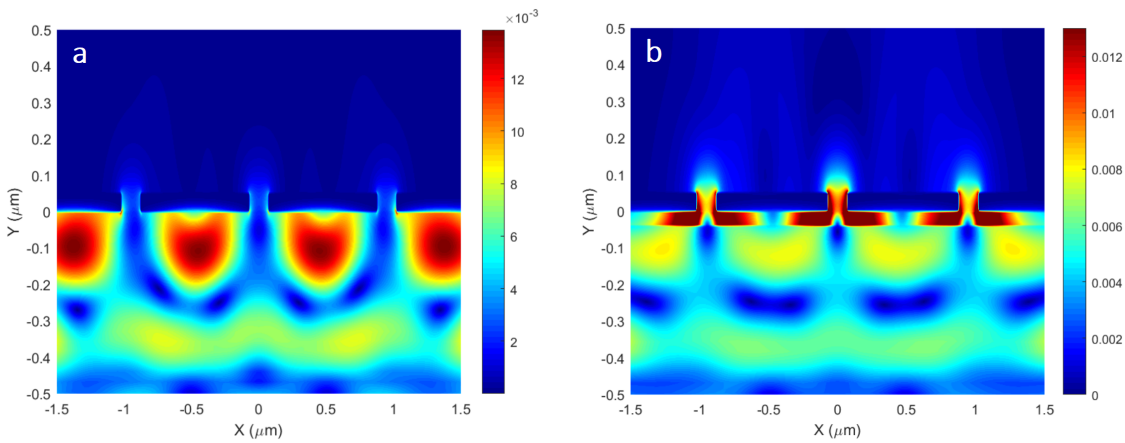

Figure 4.13. *Poynting vector magnitude from triple slits **a)** without ITO and **b)** in the presence of a 40 nm ITO layer.*

4.4 3D circular apertures

In 2D simulations for infinitely long triple slits with a 1000 nm of distance in between, a four folds enhancement in transmittance has been confirmed. However, in the proposed 3D structures maximum determined value for the enhancement factor is two times for a single ring with a 2000 nm radius. The first 3D structure that was investigated was a circular aperture. The structure was designed as a circular hole in gold with a radius varying between 150 nm to 750 nm. The transmittance achieved for a hole with a radius of less than 300 nm was negligible for experimental measurement. Because of the symmetrical shape of a circular aperture, both TE and TM modes are transmitted and this results in a smaller enhancement factor (Figure 4.14 (a)). The circular symmetry decreases the amount of enhancement by preventing of formation of dipoles, unlike a single slit. The definition of enhancement in this section remains the same as the previous part; transmittance for the sample with ITO is divided into transmittance for the sample without ITO.

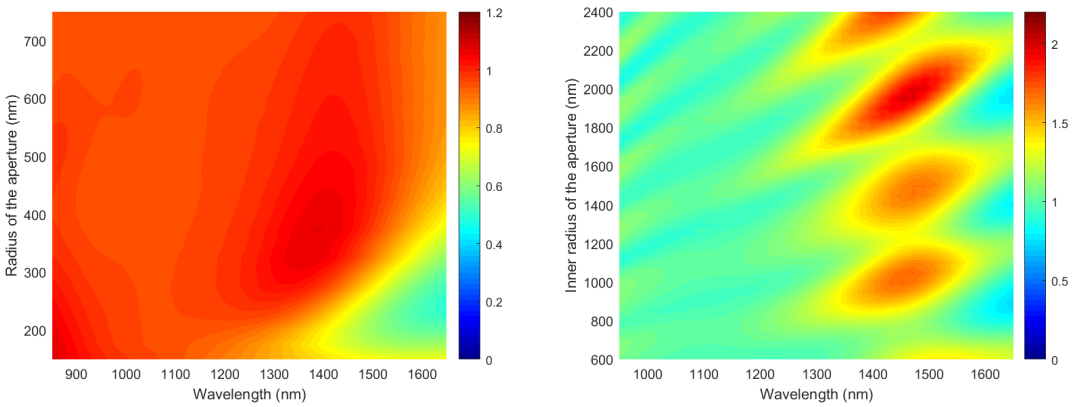

Figure 4.14. *Enhancement factor for* ***a)*** *a circular aperture* ***b)*** *a single ring.*

The main limitation for a subwavelength aperture comes from the geometrical dimension; there is an upper limit for the radius where slits lose its subwavelength nature. The upper limit radius problem in the circular aperture can be solved by keeping the central part of the shape and transforming it into a single ring.

All the phenomena discussed for a single slit and three or more slits are mostly valid in 3D circular apertures. Namely, the phase singularity correction, PSP generations by hybridizing symmetric and asymmetric modes, LSP formation inside the slit, near-field coupling (with enhancing or suppressing effects), and achieving a higher transmittance by adding more slits are the most dominant effects contributing to the EOT using ENZ materials. Three designs including a single ring with an inner radius (r) ranging from 600 to 2400 nm, a circular aperture with a fixed 370 nm radius surrounded by a ring with a variable radius, and, last by not least, a ring with a 1000 nm of inner radius, surrounded by another ring with a variable outer radius of 1500 to 4000 nm are simulated using the FDTD method. Because of the mentioned similarities with several slits, only the enhancement factors of these three structures are plotted in Figures 4.14 (b) and 4.15 (a) and (b).

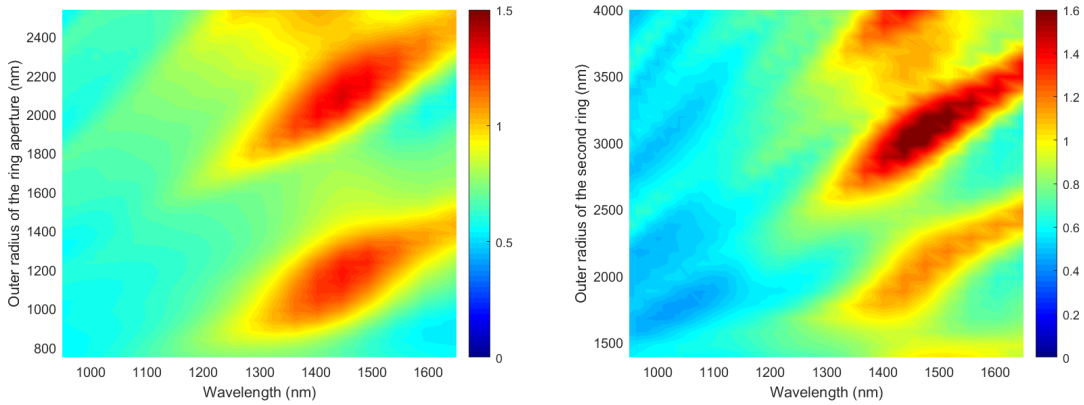

Figure 4.15. ***a)*** *Enhancement factor for a structure composed of a circle with a radius of r=370 nm and a ring with a milled width of 140 nm. The outer radius of the ring is varied between 800 nm to 2500 nm.* ***b)*** *Enhancement factor for two rings with a milled width of 140 nm. One of the rings has a 1 μm inner radius, while the outer radius of the second ring is varied between 1400 nm to 4000 nm.*

As can be observed from color bars, the single ring carries the highest importance due to the higher enhancement factor. As it is expected, this enhancement is pronounced in the ENZ region. The distance of the relative maximums in the enhancement factor is repeated in periods close to $2r$ or $\lambda_{PSP}/2$, which here lies in the spectral region around λ_{ENZ}. The highest enhancement factor in the ENZ area is reported for a ring with an inner radius of 2000 nm.

4.5 Measurements

After the design and simulation of single and triple slits, the samples with the highest expected enhancement are fabricated. Figure 4.16 shows SEM images of the fabricated single and triple slits over a 40 nm thick ITO. The fabrication process is done by milling of a 50 nm deposited gold film with the FIB machine. The fabricated slits on glass substrates and ITO/glass substrates are considered as reference and main samples, respectively. Both groups of samples are characterized by the WiTec confocal microscope by illuminating the samples with a broadband NIR beam (see Methods part for more details).

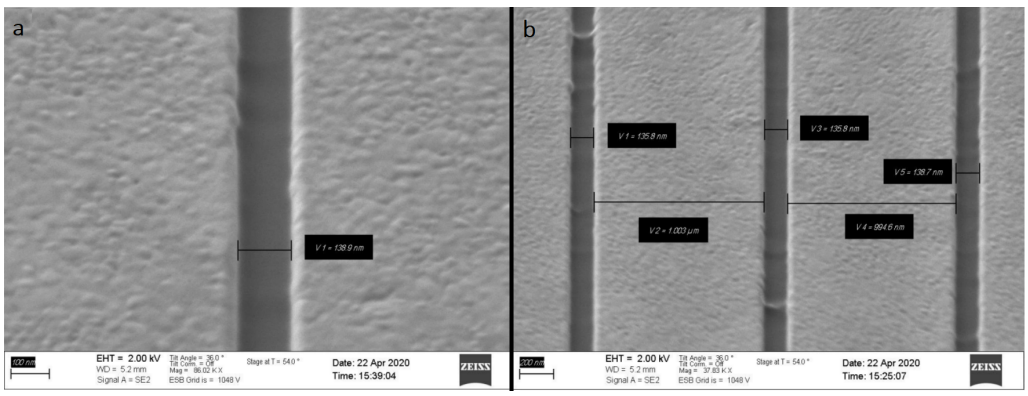

Figure 4.16. *SEM images of the fabricated samples.* ***a)*** *Single slit and* ***b)*** *triple slits.*

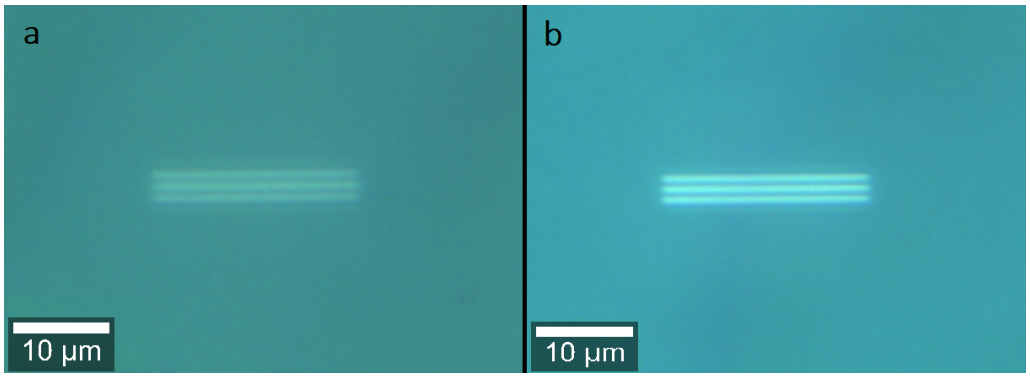

Figure 4.17. *A visible (≈500 nm) picture of the fabricated triple slit over* ***a)*** *glass,* ***b)*** *40 nm ITO film.*

The glass substrate is considered as a reference sample to measure the transmittance of all samples. The results of the implemented measurements are presented in Figure 4.18 for TM polarization of the incident beam. In this figure, the EOT effect is observed for single and triple slits. The enhancement of the transmission is stronger for triple slit compared to a single slit, regardless of the substrate type as glass or ITO/glass. However, this effect is more pronounced while the slits are fabricated over the ENZ material. An enhancement factor of 2.2 is reported for a triple slit on ITO with respect to the case that they are fabricated on the glass substrate.

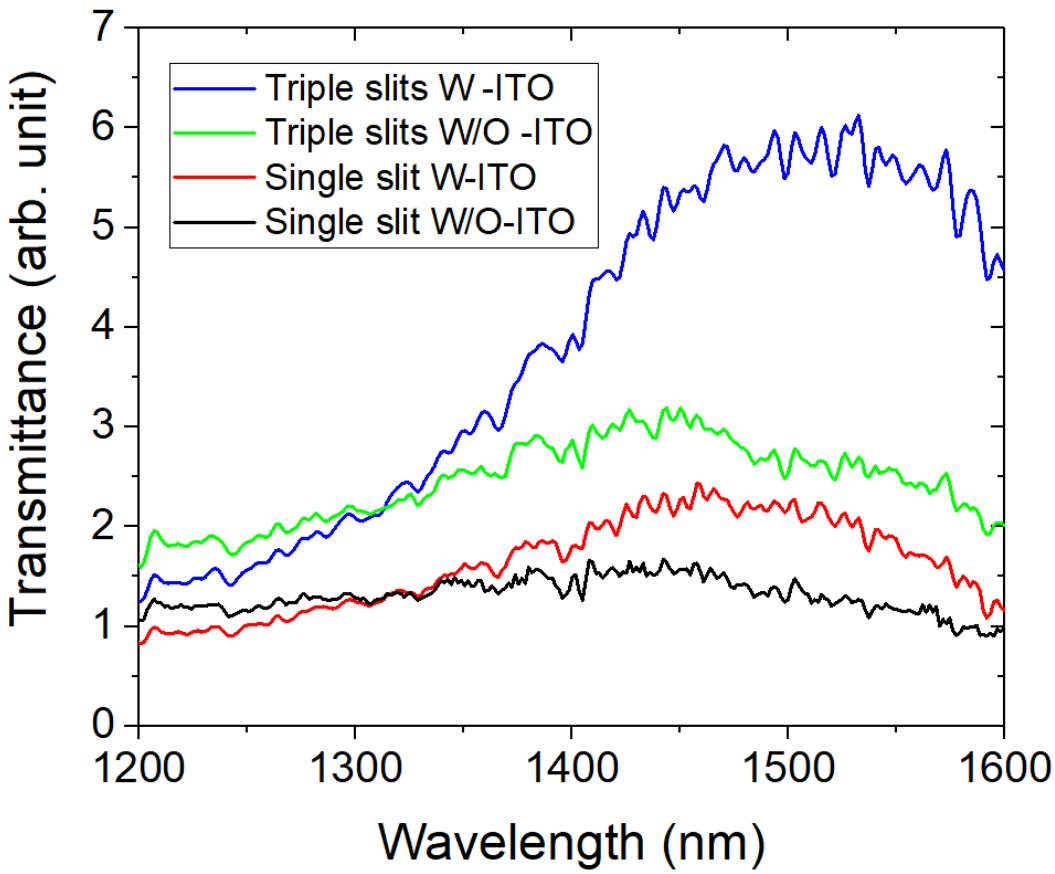

Figure 4.18. *Transmittance of TM polarized light through single and triple slits.*

The enhancement factor difference in simulation and experimental results can be attributed to the deviation in the fabrication process and measurement system. The spectral position of the enhanced transmission band is consistent with the simulation results. The characterization results of the fabricated samples for TE polarization of the incident light are presented in Figure 4.19. The comparison of the acquired results for TE and TM polarizations proves that the enhancement of the transmission only occurs for the incident beam with TM polarization state, which is in agreement with the discussed theory in former sections.

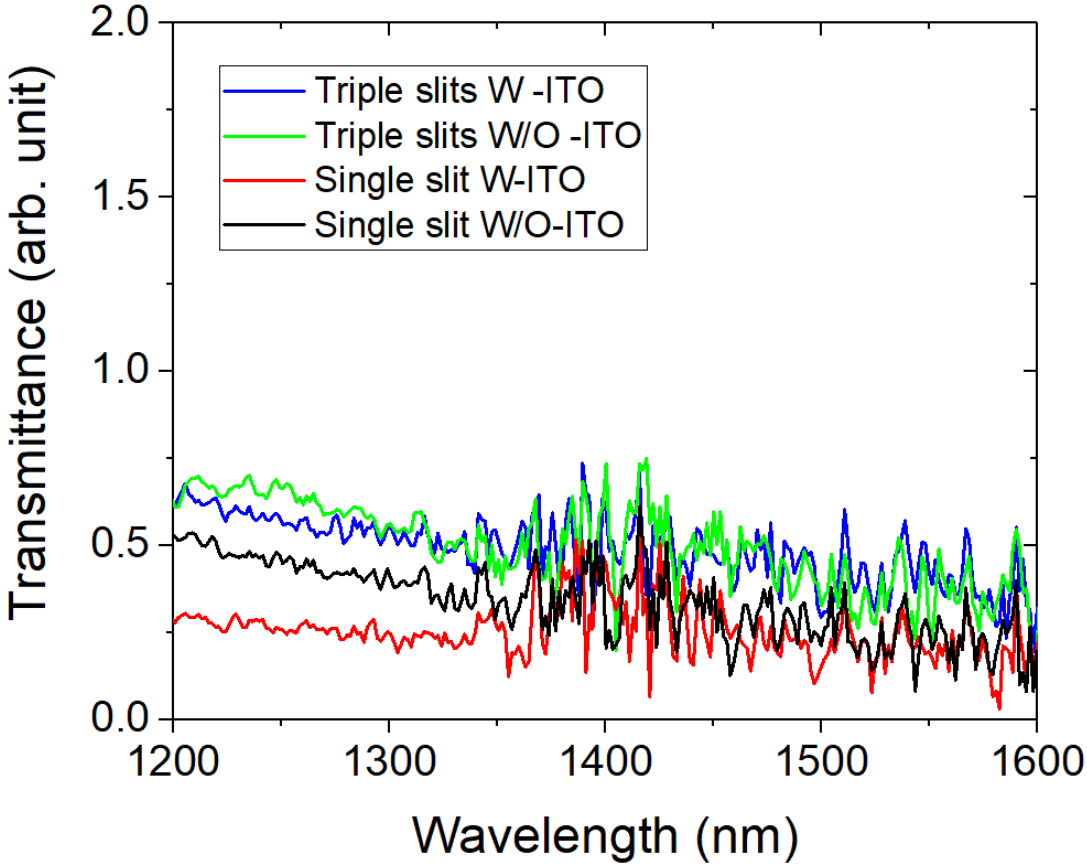

Figure 4.19. *Transmittance of TE polarized light through single and triple slits.*

5 CONCLUSION

In this thesis, the possibility of harnessing ENZ material's capabilities in favor of an EOT for different apertures is proven. First, the ENZ region is determined for a particular fabricated ITO layer over the glass. Then, simulations are done and the transmittance enhancement factor is calculated for a single slit, three slits, a circular aperture, a single ring, and two rings (non intercepting). The benefits of adding an ITO layer and physical interpretation of observed phenomena are explored. Poynting vector, Electric field, and field intensity behavior are investigated around a subwavelength slit.

According to this study, the prominent effect of adding an ITO layer to a subwavelength structure is attributed to the engineered phase. A new explanation for the EOT after adding the ITO layer is established using phase preservation and field enhancement in this layer. The reason can be sought in the annihilation of phase singularities, which leads to smoother adjacent fields around the slit, resulting in the achieved enhancement. Other known effects such as PSP generations from the hybridization of symmetric and asymmetric modes, LSP (i.e., cavity mode) formation inside the slit, enhancement and suppression of the near-field coupling, and achieving a higher transmittance by adding more slits are summed up in a nutshell.

This work included the fabrication of two designs ,namely, single and triple slits. The transmittance of the fabricated samples is measured using a confocal microscope. Transmittance results are in good agreement with predictions and simulations. However, due to imperfections of the fabrication compared to the designed system, the enhancement effect was partially concealed. Fabrication of several slits (more than four) and other 3D apertures remains as an open chapter for further studies.

The high potential of EOT can be liberated using a thorough understanding of all the involving physical phenomena. Due to the short history of studies, including EOT, there is room for both theoretical and physical investigations, especially for more complex systems and new structural designs.

REFERENCES

[1] Bethe, H. A. Theory of diffraction by small holes. *Physical review* 66.7-8 (1944), 163.

[2] Maier, S. A. *Plasmonics: fundamentals and applications*. Springer Science & Business Media, 2007.

[3] Hajian, H., Ozbay, E. and Caglayan, H. Beaming and enhanced transmission through a subwavelength aperture via epsilon-near-zero media. *Scientific Reports* 7.1 (June 2017). DOI: 10.1038/s41598-017-04680-y.

[4] Orfanidis, S. J. *Electromagnetic Waves and Antennas*. Rutgers University, 2016, 3–6.

[5] Tom G. Mackay, A. L. *Electromagnetic Anisotropy and Bianisotropy: A Field Guide*. World Scientific, 2009, iv–40.

[6] Weiner, J. and Nunes, F. D. *Light-matter interaction: physics and engineering at the nanoscale*. 2nd ed. Oxford University Press, 2017.

[7] Weiner, J. and Nunes, F. D. *Light-matter interaction: physics and engineering at the nanoscale*. Oxford University Press, 2013.

[8] Larson, D. B. and Larson, D. B. *The structure of the physical universe*. North Pacific Publ., 1979.

[9] Rahimi, A. *Absorpitive losses mitigation in gain-plasmon hybrid systems as optical metamaterials*. Nov. 2013. URL: http://hdl.handle.net/10955/1007.

[10] Madou, M. J. *Fundamentals of microfabrication and nanotechnology*. CRC Press, 2018.

[11] Purcell, E. M. *Electricity and magnetism*. Cambridge University Press, 2013.

[12] Bertrand, P., Del Sarto, D. and Ghizzo, A. *The Vlasov Equation: History and General Properties*. 2019.

[13] Levi, A. F. J. *Applied quantum mechanics*. Cambridge University Press, 2012.

[14] *Harmonic Waves*. URL: https://home.jbnu.ac.kr/_ezaid/board/genBoardRecord.ez?method=download&pfkHomepageNo=1409&fkBoardEntryPkNo=11&attacheFileChoice=5&pkNo=2399.

[15] Yeh, P. *Optical waves in layered media*. Wiley-Interscience, 2005.

[16] Richmond, M. *Phase and group velocities*. URL: http://spiff.rit.edu/classes/phys283/lectures/velocities/velocities.html.

[17] Stratton, J. A. *Electromagnetic theory*. Vol. 33. John Wiley & Sons, 2007.

[18] Feynman, R. P. Feynman lectures on physics. Volume 2: Mainly electromagnetism and matter. *Reading, Ma.: Addison-Wesley, 1964, edited by Feynman, Richard P.; Leighton, Robert B.; Sands, Matthew* (1964).

[19] Smith, B. C. *Fundamentals of Fourier transform infrared spectroscopy*. CRC Press, 2011.

[20] Shi, K. and Lu, Z. Field-effect optical modulation based on epsilon-near-zero conductive oxide. *Optics Communications* 370 (2016), 22–28. ISSN: 0030-4018. DOI: https://doi.org/10.1016/j.optcom.2016.02.062. URL: http://www.sciencedirect.com/science/article/pii/S0030401816301559.

[21] Li, X. Epsilon-near-zero Metamaterials for Optoelectronic Applications. PhD thesis. University of St Andrews, 2019.

[22] Paschotta, R. *Phase Velocity*. Mar. 2020. URL: https://www.rp-photonics.com/phase_velocity.html.

[23] Acharya, R. *Satellite signal propagation, impairments and mitigation*. Academic Press, 2017.

[24] Smith, D. R. *Plasmonics: Enhancement*. URL: http://people.ee.duke.edu/~drsmith/plasmonics/enhancement.htm.

[25] Engheta, N. Pursuing Near-Zero Response. *Science* 340.6130 (2013), 286–287. DOI: 10.1126/science.1235589. URL: https://science.sciencemag.org/content/340/6130/286.

[26] Tricker, R. A. and Cenedese, C. *Wave*. Oct. 2018. URL: https://www.britannica.com/science/wave-water#ref180109.

[27] Stockman, M. I. Criterion for Negative Refraction with Low Optical Losses from a Fundamental Principle of Causality. *Physical Review Letters* 98.17 (2007). DOI: 10.1103/physrevlett.98.177404. URL: https://journals.aps.org/prl/pdf/10.1103/PhysRevLett.98.177404.

[28] Lucarini, V. *Kramers Kronig relations in optical materials research*. Springer, 2010.

[29] Vesseur, E. J. R., Coenen, T., Caglayan, H., Engheta, N. and Polman, A. Experimental Verification of n=0 Structures for Visible Light. *Physical Review Letters* 110.1 (Feb. 2013). DOI: 10.1103/physrevlett.110.013902. URL: https://physics.aps.org/featured-article-pdf/10.1103/PhysRevLett.110.013902.

[30] Javani, M. H. and Stockman, M. I. Real and Imaginary Properties of Epsilon Near Zero Materials. *Physical Review Letters* 117.10 (Feb. 2016). DOI: 10.1103/physrevlett.117.107404.

[31] Landivar, V. T. Plasmonics and Metamaterials at Terahertz Frequencies. PhD thesis. 2014.

[32] Jackson, J. D. *Classical electrodynamics*. Wiley, 2016.

[33] Cai, W. Metal Coated Waveguide Stretches Wavelengths to Infinity. *Physics* 6 (Feb. 2013). DOI: 10.1103/physics.6.1. URL: https://physics.aps.org/articles/pdf/10.1103/Physics.6.1.

[34] Duan, X., Zhang, F., Qian, Z., Hao, H., Shan, L., Gong, Q. and Gu, Y. Accumulation and directionality of large spontaneous emission enabled by epsilon near zero film. *Optics Express* 27.5 (2019). DOI: 10.1364/fio.2019.jw4a.69.

[35] Fu, Y., Xu, L., Hang, Z. H. and Chen, H. Unidirectional transmission using array of zero refractive index metamaterials. *Applied Physics Letters* 104.19 (Dec. 2014), 193509. DOI: 10.1063/1.4878400. URL: https://aip.scitation.org/doi/full/10.1063/1.4878400.

[36] Wang, B. and Huang, K. Shaping The Radiation Pattern With Mu And Epsilon Near Zero Metamaterials. *Progress In Electromagnetics Research* 106 (2010), 107–119. DOI: 10.2528/pier10060103.

[37] Jenkins, F. A. and White, H. E. *Fundamentals of optics*. Mc Graw-Hill Primis Custom Publ., 1976.

[38] PRELOG, V. *CHIRALITY IN CHEMISTRY (Nobel Lecture)*. Dec. 1975.

[39] Wang, Z., Chong, Y., Joannopoulos, J. D. and Soljačić, M. Observation of unidirectional backscattering immune topological electromagnetic states. *Nature* 461.7265 (2009), 772–775. DOI: 10.1038/nature08293. URL: https://www.ncbi.nlm.nih.gov/pubmed/19812669.

[40] Karimullah, A. S., Jack, C., Tullius, R., Rotello, V. M., Cooke, G., Gadegaard, N., Barron, L. D. and Kadodwala, M. Disposable Plasmonics: Plastic Templated Plasmonic Metamaterials with Tunable Chirality. *Advanced Materials* 27.37 (2015), 5610–5616. DOI: 10.1002/adma.201501816.

[41] Rizza, C., Li, X., Di Falco, A., Palange, E., Marini, A. and Ciattoni, A. Optical chiral effects in ENZ ultrathin slabs. Feb. 2018.

[42] Rizza, C., Falco, A. D., Scalora, M. and Ciattoni, A. One Dimensional Chirality: Strong Optical Activity in Epsilon Near Zero Metamaterials. *Physical Review Letters* 115.5 (2015). DOI: 10.1103/physrevlett.115.057401. URL: https://journals.aps.org/prl/abstract/10.1103/PhysRevLett.115.057401.

[43] Pramodini, S. Third order optical nonlinearity and optical power limiting of organic materials under CW laser illumination. PhD thesis. 2015.

[44] Yariv, A. The application of time evolution operators and Feynman diagrams to nonlinear optics. *IEEE Journal of Quantum Electronics* 13.12 (1977), 943–950. DOI: 10.1109/jqe.1977.1069267. URL: https://authors.library.caltech.edu/9833/1/YARieeejqe77b.pdf.

[45] Brewer, R. G. and Hahn, E. L. Coherent two photon processes: Transient and steady state cases. *Physical Review A* 11.5 (Jan. 1975), 1641–1649. DOI: 10.1103/physreva.11.1641. URL: https://journals.aps.org/pra/abstract/10.1103/PhysRevA.11.1641.

[46] Noblet, T. and Humbert, C. *Sum-frequency generation through a unique Feynman diagram formalism: the case of bipartite organic/inorganic complexes*. 2019. arXiv: 1906.03197 [physics.optics].

[47] Shen, Y. R. *The Principles of Nonlinear Optics (WCL)*. 1st ed. John Wiley and Sons, 2002.

[48] Ward, J. F. Calculation of Nonlinear Optical Susceptibilities Using Diagrammatic Perturbation Theory. *Reviews of Modern Physics* 37.1 (Jan. 1965), 1–18. DOI: 10.1103/revmodphys.37.1.

[49] Lembrikov, B. I. Introductory Chapter: Nonlinear Optical Phenomena. *Nonlinear Optics Novel Results in Theory and Applications* (June 2019). DOI: 10.5772/intechopen.83718. URL: https://www.intechopen.com/books/nonlinear-

optics-novel-results-in-theory-and-applications/introductory-chapter-nonlinear-optical-phenomena.

[50] Suhara, T. and Fujimura, M. *Waveguide nonlinear optic devices*. Springer, 2003.

[51] Caspani, L., Kaipurath, R., Clerici, M. and, e. al et. Enhanced Nonlinear Refractive Index in eps Near Zero Materials. *Physical Review Letters* 116.23 (June 2016). URL: https://journals.aps.org/prl/abstract/10.1103/PhysRevLett.116.233901.

[52] Kinsey, N. and Khurgin, J. Nonlinear epsilon-near-zero materials explained: opinion. *Optical Materials Express* 9.7 (June 2019), 2793. DOI: 10.1364/ome.9.002793. URL: https://www.osapublishing.org/ome/abstract.cfm?uri=ome-9-7-2793.

[53] Terhune, R., Maker, P. and Savage, C. Nonlinear effects has numerous applications as transient coherent effect, optical harmonic generation and self-focusing of optical beams. *Physical Review Letters 8, 404* (1962).

[54] Kelley, P. L. Self Focusing of Optical Beams. *Physical Review Letters* 15.26 (1965), 1005–1008. DOI: 10.1103/physrevlett.15.1005. URL: https://journals.aps.org/prl/abstract/10.1103/PhysRevLett.15.1005.

[55] Eilbeck, J. C. and Bullough, R. K. The method of characteristics in the theory of resonant or nonresonant nonlinear optics. *Journal of Physics A: General Physics* 5.6 (Jan. 1972), 820–829. DOI: 10.1088/0305-4470/5/6/007. URL: https://iopscience.iop.org/article/10.1088/0305-4470/5/6/007.

[56] Wang, Y. Nonlinear optical properties of nanometer sized semiconductor clusters. *Accounts of Chemical Research* 24.5 (1991), 133–139. DOI: 10.1021/ar00005a002. URL: https://pubs.acs.org/doi/abs/10.1021/ar00005a002.

[57] Pendry, J. B. Negative Refraction Makes a Perfect Lens. *Physical Review Letters* 85.18 (2000), 3966–3969. DOI: 10.1103/physrevlett.85.3966. URL: https://journals.aps.org/prl/abstract/10.1103/PhysRevLett.85.3966.

[58] Mahmoud, A. M. A. Wave Interaction With Epsilon and Mu Near Zero (emnz) Platforms and Nonreciprocal Metastructures. PhD thesis. University of Pennsylvania, 2016.

[59] Silveirinha, M. and Engheta, N. Tunneling of Electromagnetic Energy through Subwavelength Channels and Bends using eps Near Zero Materials. *Physical Review Letters* 97.15 (Oct. 2006). DOI: 10.1103/physrevlett.97.157403. URL: https://journals.aps.org/prl/abstract/10.1103/PhysRevLett.97.157403.

[60] Alù, A. G., Silveirinha, M. G., Salandrino, A. G. and Engheta, N. G. Epsilon-near-zero metamaterials and electromagnetic sources: Tailoring the radiation phase pattern. *Physical Review B* 75.15 (Nov. 2007). DOI: 10.1103/physrevb.75.155410. URL: https://journals.aps.org/prb/abstract/10.1103/PhysRevB.75.155410.

[61] Landy, N. I., Sajuyigbe, S., Mock, J. J., Smith, D. R. and Padilla, W. J. *Perfect Metamaterial Absorber*. May 2008. URL: https://journals.aps.org/prl/abstract/10.1103/PhysRevLett.100.207402.

[62] Jin, Y., Xiao, S. and Mortensen, N. A. *Arbitrarily thin metamaterial structure for perfect absorption and giant magnification*. May 2011. URL: https://www.osapublishing.org/oe/abstract.cfm?uri=oe-19-12-11114.

[63] Badsha, M. A., Jun, Y. C. and Hwangbo, C. K. *Admittance matching analysis of perfect absorption in unpatterned thin films*. July 2014. URL: https://www.sciencedirect.com/science/article/pii/S0030401814006221.

[64] Wang, Z., Zhou, P. and Zheng, G. *Electrically switchable highly efficient epsilon-near-zero metasurfaces absorber with broadband response*. May 2019. URL: https://www.sciencedirect.com/science/article/pii/S2211379719310034.

[65] Yoon, J., Zhou, M., Badsha, M. A., Kim, T. Y., Jun, Y. C. and Hwangbo, C. K. *Broadband Epsilon-Near-Zero Perfect Absorption in the Near-Infrared*. Aug. 2015. URL: https://www.nature.com/articles/srep12788.

[66] Kasap, S. and Capper, P. *Springer handbook of electronic and photonic materials*. Springer, 2017.

[67] Naik, G. V., Kim, J. and Boltasseva, A. *Oxides and nitrides as alternative plasmonic materials in the optical range [Invited]*. Oct. 2011. URL: https://www.osapublishing.org/ome/abstract.cfm?URI=ome-1-6-1090.

[68] Hecht, D. S., Hu, L. and Irvin, G. Emerging Transparent Electrodes Based on Thin Films of Carbon Nanotubes, Graphene, and Metallic Nanostructures. *Advanced Materials* 23.13 (2011), 1482–1513. DOI: 10.1002/adma.201003188.

[69] Stadler, A. Transparent Conducting Oxides—An Up-To-Date Overview. *Materials* 5.12 (2012), 661–683. DOI: 10.3390/ma5040661.

[70] Bakish, R. A. *50 years of Vacuum Coating technology and the growth of the Society of Vacuum Coaters*. Society of Vacuum Coaters, 2007.

[71] Chavan, S., Foulkes, T., Gurumukhi, Y., Boyina, K., Rabbi, K. F. and Miljkovic, N. Pulse interfacial defrosting. *Applied Physics Letters* 115.7 (Dec. 2019), 071601. DOI: 10.1063/1.5113845. URL: https://aip.scitation.org/doi/10.1063/1.5113845.

[72] Füchsel, K., Schulz, U., Kaiser, N. and Tünnermann, A. *Low temperature deposition of indium tin oxide films by plasma ion-assisted evaporation*. Feb. 2008. URL: https://www.osapublishing.org/ao/abstract.cfm?uri=ao-47-13-c297.

[73] Hartnagel, H., Dawar, A. and Jain, A. *Semiconducting transparent thin films*. IOP, 1995.

[74] Maruyama, T. and Kojima, A. Indium-Tin Oxide Thin Films Prepared by Thermal Decomposition of Metallic Complex Salts. *Japanese Journal of Applied Physics* 27.Part 2, No. 10 (1988). DOI: 10.1143/jjap.27.l1829. URL: https://iopscience.iop.org/article/10.1143/JJAP.27.L1829/meta.

[75] Mahajeri, M., Schneider, A., Baum, M., Rechtenwald, T., Voigt, M., Schmidt, M. and Peukert, W. Production of dispersions with small particle size from commercial indium tin oxide powder for the deposition of highly conductive and transparent films. *Thin Solid Films* 520 (June 2012), 5741–5745. DOI: 10.1016/j.tsf.2012.03.121.

[76] Gonçalves, G., Elamurugu, E., Barquinha, P., Pereira, L., Martins, R. and Fortunato, E. Influence of Post-Annealing Temperature on the Properties Exhibited by ITO IZO and GZO Thin Films. *Thin Solid Films* 515 (Oct. 2007), 8562–8566. DOI: 10.1016/j.tsf.2007.03.126.

[77] *National Minerals Information Center*. URL: http://minerals.usgs.gov/minerals/pubs/commodity/indium/mcs-2009-indiu.pdf%20report.

[78] Ginley, D. S. *Handbook of Transparent Conductors*. Springer US, 2010.

[79] Kim, J., Naik, G. V., Gavrilenko, A. V., Dondapati, K., Gavrilenko, V. I., Prokes, S. M., Glembocki, O. J., Shalaev, V. M. and Boltasseva, A. *Optical Properties of Gallium-Doped Zinc Oxide—A Low-Loss Plasmonic Material: First-Principles Theory and Experiment*. Dec. 2013. URL: https://journals.aps.org/prx/abstract/10.1103/PhysRevX.3.041037.

[80] Rashed, A. R., Gudulluoglu, B., Yun, H. W., Habib, M., Boyaci, I. H., Hong, S. H., Ozbay, E. and Caglayan, H. *Highly-Sensitive Refractive Index Sensing by Near-infrared Metatronic Nanocircuits*. July 2018. URL: https://www.nature.com/articles/s41598-018-29623-z.

[81] Guo, Yu, Newman, Ward, Cortes, L., C., Jacob and Zubin. *Applications of Hyperbolic Metamaterial Substrates*. Dec. 2012. URL: https://www.hindawi.com/journals/aoe/2012/452502/.

[82] Rashed, A. R., Yildiz, B. C., Ayyagari, S. R. and Caglayan, H. Hot electron dynamics in ultrafast multilayer epsilon-near-zero metamaterials. *Phys. Rev. B* 101 (16 Apr. 2020), 165301. DOI: 10.1103/PhysRevB.101.165301. URL: https://link.aps.org/doi/10.1103/PhysRevB.101.165301.

[83] Weiglhofer, W., Lakhtakia, A. and Michel, B. Maxwell Garnett and Bruggeman Formalisms for Particulate Composite with Bianisotropic Host Medium. *Microwave and Optical Technology Letters - MICROWAVE OPT TECHNOL LETT* 22 (Aug. 1999), 221. DOI: 10.1002/(SICI)1098-2760(19990805)22:33.0.CO;2-R.

[84] Gennaro, S. D. and Oulton, R. F. PhD thesis. IMPERIAL COLLEGE LONDON DEPARTMENT OF PHYSICS, 2015.

[85] Rivera, V. A. G., Ferri, F. A., Silva, O. B., Sobreira, F. W. A. and Jr., E. M. Light Transmission via Subwavelength Apertures in Metallic Thin Films. *Plasmonics*. Ed. by K. Y. Kim. Rijeka: IntechOpen, 2012. Chap. 7. DOI: 10.5772/50807. URL: https://doi.org/10.5772/50807.

[86] Bouwkamp, C. J. Diffraction theory. *Reports on progress in physics* 17.1 (1954), 35.

[87] Weiner, J. The physics of light transmission through subwavelength apertures and aperture arrays. *Reports on progress in physics* 72.6 (2009), 064401.

[88] Bilotti, F., Scorrano, L., Alici, K. B., Aydin, K., Cakmak, O. A., Ozbay, E. and Vegni, L. Enhanced transmission through sub-wavelength apertures by using metamaterials. *Selected Topics in Photonic Crystals and Metamaterials*. World Scientific, 2011, 453–477.

[89] Dennis, M. R., O'Holleran, K. and Padgett, M. J. Singular optics: optical vortices and polarization singularities. *Progress in optics*. Vol. 53. Elsevier, 2009, 293–363.

[90] Schouten, H. F., Visser, T. D. and Lenstra, D. Optical vortices near sub-wavelength structures. *Journal of Optics B: Quantum and Semiclassical Optics* 6.5 (2004), S404.

[91] Schouten, H. F., Visser, T. D., Lenstra, D. and Blok, H. Light transmission through a subwavelength slit: Waveguiding and optical vortices. *Physical Review E* 67.3 (2003), 036608.

[92] Schouten, H. F., Visser, T. D., Gbur, G., Lenstra, D. and Blok, H. The diffraction of light by narrow slits in plates of different materials. *Journal of Optics A: Pure and Applied Optics* 6.5 (2004), S277.

[93] Chen, S., Li, Z., Zhang, Y., Cheng, H. and Tian, J. Phase manipulation of electromagnetic waves with metasurfaces and its applications in nanophotonics. *Advanced Optical Materials* 6.13 (2018), 1800104.

[94] Garcia-Vidal, F., Lezec, H., Ebbesen, T. and Martin-Moreno, L. Multiple paths to enhance optical transmission through a single subwavelength slit. *Physical Review Letters* 90.21 (2003), 213901.

[95] Laluet, J.-Y., Drezet, A., Genet, C. and Ebbesen, T. Generation of surface plasmons at single subwavelength slits: from slit to ridge plasmon. *New Journal of Physics* 10.10 (2008), 105014.

[96] Kiyan, R., Reinhardt, C., Passinger, S., Stepanov, A. L., Hohenau, A., Krenn, J. R. and Chichkov, B. N. Rapid prototyping of optical components for surface plasmon polaritons. *Optics express* 15.7 (2007), 4205–4215.

[97] Chang, S.-H. and Su, Y.-L. Mapping of transmission spectrum between plasmonic and nonplasmonic single slits. II: nonresonant transmission. *JOSA B* 32.1 (2015), 45–51.

[98] Ferri, F. A., Rivera, V. A., Osorio, S. P., Silva, O. B., Zanatta, A. R., Borges, B.-H. V., Weiner, J. and Marega Jr, E. Influence of film thickness on the optical transmission through subwavelength single slits in metallic thin films. *Applied optics* 50.31 (2011), G11–G16.

[99] Li, J.-W., Hong, J.-S., Chou, W.-T., Huang, D.-J. and Chen, K.-R. Light Funneling Profile During Enhanced Transmission Through a Subwavelength Metallic Slit. *Plasmonics* 13 (Mar. 2018), 2249–2254. DOI: 10.1007/s11468-018-0745-z.

[100] Chen, Y. and Ming, H. Review of surface plasmon resonance and localized surface plasmon resonance sensor. *Photonic Sensors* 2.1 (2012), 37–49.

[101] Raether, H. *Surface plasmons on smooth and rough surfaces and on gratings*. Springer-Verlag Berlin An, 2013.

[102] Li, L. *Manipulation of near field propagation and far field radiation of surface plasmon polariton*. Springer, 2017.

[103] El Kabbash, M., Rahimi Rashed, A., Sreekanth, K. V., De Luca, A., Infusino, M. and Strangi, G. Plasmon-exciton resonant energy transfer: across scales hybrid systems. *Journal of Nanomaterials* 2016 (2016).

[104] Park, T.-H., Mirin, N., Lassiter, J. B., Nehl, C. L., Halas, N. J. and Nordlander, P. Optical properties of a nanosized hole in a thin metallic film. *Acs Nano* 2.1 (2008), 25–32.

[105] Wang, H., Brandl, D. W., Nordlander, P. and Halas, N. J. Plasmonic nanostructures: artificial molecules. *Accounts of chemical research* 40.1 (2007), 53–62.

[106] Prodan, E., Radloff, C., Halas, N. J. and Nordlander, P. A hybridization model for the plasmon response of complex nanostructures. *science* 302.5644 (2003), 419–422.

[107] Gadalla, M. N., Chaudhary, K., Zgrabik, C. M., Capasso, F. and Hu, E. L. Imaging of surface plasmon polaritons in low-loss highly metallic titanium nitride thin films in visible and infrared regimes. *Optics Express* 28.10 (2020), 14536–14546.

[108] Yildiz, B. C., Rashed, A. and Caglayan, H. Loss compensated extraordinary transmission in hybridized plasmonic nanocavities. *Journal of Optics* (2020).

[109] Lezec, H. J., Degiron, A., Devaux, E., Linke, R. A., Martin-Moreno, L., Garcia-Vidal, F. J. and Ebbesen, T. W. Beaming Light from a Subwavelength Aperture. *Science* 297.5582 (2002), 820–822. ISSN: 0036-8075. DOI: 10.1126/science.1071895. eprint: https://science.sciencemag.org/content/297/5582/820.full.pdf. URL: https://science.sciencemag.org/content/297/5582/820.

[110] Ebbesen, T. W., Lezec, H. J., Ghaemi, H., Thio, T. and Wolff, P. A. Extraordinary optical transmission through sub-wavelength hole arrays. *Nature* 391.6668 (1998), 667–669.

[111] Jiao, X.-J., Tang, L., Wang, P., Lu, Y.-H., Li, Q., Zhang, D.-G., Yao, P., Ming, H. and Xie, J. The role of surface plasmon polaritons in the transmission of the light through different periodic structures in the metal film. *Nanophotonics, Nanostructure, and Nanometrology*. Vol. 5635. International Society for Optics and Photonics. 2005, 361–365.

[112] Watts, R., Harris, J., Hibbins, A., Preist, T. and Sambles, J. Optical excitation of surface plasmon polaritons on 90 and 60 bi-gratings. *journal of modern optics* 43.7 (1996), 1351–1360.

[113] Yanik, A. A., Adato, R., Erramilli, S. and Altug, H. Hybridized nanocavities as single-polarized plasmonic antennas. *Optics express* 17.23 (2009), 20900–20910.

[114] Hajian, H., Ozbay, E. and Caglayan, H. Beaming and enhanced transmission through a subwavelength aperture via epsilon-near-zero media. *Scientific reports* 7.1 (2017), 1–8.

[115] Olkkonen, J. *Finite difference time domain studies on sub-wavelength aperture structures*. VTT, 2010.

[116] Yee, K. Numerical solution of initial boundary value problems involving Maxwell's equations in isotropic media. *IEEE Transactions on antennas and propagation* 14.3 (1966), 302–307.

[117] Johnson, P. B. and Christy, R.-W. Optical constants of the noble metals. *Physical review B* 6.12 (1972), 4370.

[118] Bruno, V., DeVault, C., Vezzoli, S., Kudyshev, Z., Huq, T., Mignuzzi, S., Jacassi, A., Saha, S., Shah, Y., Maier, S. et al. Negative Refraction in Time-Varying Strongly Coupled Plasmonic-Antenna–Epsilon-Near-Zero Systems. *Physical Review Letters* 124.4 (2020), 043902.

[119] Ahmadi, S., Asim, N., Alghoul, M., Hammadi, F., Saeedfar, K., Ludin, N. A., Zaidi, S. H. and Sopian, K. The role of physical techniques on the preparation of photoanodes for dye sensitized solar cells. *International Journal of Photoenergy* 2014 (2014).

[120] Harsha, K. S. *Principles of vapor deposition of thin films*. Elsevier, 2005.

[121] Selcuk, S. *Optical studies of subwavelength structures*. University of Florida Doctoral dissertation, 2008.

[122] Fürjes, P. Controlled Focused Ion Beam Milling of Composite Solid State Nanopore Arrays for Molecule Sensing. *Micromachines* 10.11 (2019), 774.

[123] Schouten, H. F., Visser, T. D., Gbur, G., Lenstra, D. and Blok, H. Creation and annihilation of phase singularities near a sub-wavelength slit. *Optics Express* 11.4 (2003), 371. DOI: 10.1364/oe.11.000371. URL: https://www.osapublishing.org/oe/abstract.cfm?uri=oe-11-4-371.

[124] Adams, D., Inampudi, S., Ribaudo, T., Slocum, D., Vangala, S., Kuhta, N., Goodhue, W., Podolskiy, V. A. and Wasserman, D. Funneling light through a subwavelength aperture with epsilon-near-zero materials. *Physical Review letters* 107.13 (2011), 133901.

[125] Xie, Y., Zakharian, A. R., Moloney, J. V. and Mansuripur, M. Transmission of light through slit apertures in metallic films. *Optics express* 12.25 (2004), 6106–6121.

[126] Huang, X., Peng, R., Wang, Z., Gao, F. and Jiang, S. Charge-oscillation-induced light transmission through subwavelength slits and holes. *Physical Review A* 76.3 (2007), 035802.

[127] Seo, M., Park, H., Koo, S., Park, D., Kang, J., Suwal, O., Choi, S., Planken, P., Park, G., Park, N. et al. Terahertz field enhancement by a metallic nano slit operating beyond the skin-depth limit. *Nature Photonics* 3.3 (2009), 152.

[128] Kong, J. A. *Electromagnetic wave theory*. EMW Publ., 2008.

[129] Okamoto, K. *Fundamentals of Optical Waveguides*. Elsevier/Academic Press, 2011.

[130] Zhou, R., Chen, X., Wang, S., Lu, W., Zeng, Y., Chen, H., Li, H., Xia, H. and Wang, L. The surface plasmon resonance of metal-film nanohole arrays. *Solid state communications* 145.1-2 (2008), 23–28.

[131] Pacifici, D., Lezec, H., Atwater, H. A. and Weiner, J. Quantitative determination of optical transmission through subwavelength slit arrays in Ag films: Role of surface wave interference and local coupling between adjacent slits. *Physical Review B* 77.11 (2008), 115411.

[132] Chen, L., Robinson, J. T. and Lipson, M. Role of radiation and surface plasmon polaritons in the optical interactions between a nano-slit and a nano-groove on a metal surface. *Optics express* 14.26 (2006), 12629–12636.

[133] Kalkum, F., Gay, G., Alloschery, O., Weiner, J., Lezec, H., Xie, Y. and Mansuripur, M. Surface-wave interferometry on single subwavelength slit-groove structures fabricated on gold films. *Optics express* 15.5 (2007), 2613–2621.

[134] Ung, B. and Sheng, Y. Optical surface waves over metallo-dielectric nanostructures: Sommerfeld integrals revisited. *Optics express* 16.12 (2008), 9073–9086.